Studies on Mixed Slab-Toroidal Electron Temperature Gradient Mode Instabilities in the Columbia Linear Machine

Abed Balbaky

Submitted in partial fulfillment of the

requirements for the degree of

Doctor of Philosophy

in the Graduate School of Arts and Sciences

COLUMBIA UNIVERSITY

2015

Abstract

Studies on Mixed Slab-Toroidal Electron Temperature Gradient Mode Instabilities in the Columbia Linear Machine

Abed Balbaky

This thesis investigates the behavior of electron temperature gradient (ETG) driven instabilities in the Columbia Linear Machine (CLM). Building on prior work in CLM, the primary goal of this research is to produce, identify, and illuminate the basic physics of these instabilities, and explore the behavior of these instabilities under the presence of trapping and curved magnetic field lines.

The first part of this thesis is focused on studying the saturated ETG mode, and the general behavior of the mode under varying levels of magnetic curvature. Measuring ETG modes can be problematic since they have large real frequencies, fast growth rates (~MHz) and small spatial scales, but carefully designed probe diagnostics can overcome these limits. In order to produce curved magnetic field lines, we modified CLM to operate with an internal movable mirror coil. We determined the temperature and density profiles under varying curvature, and measured changes in the mode structure and frequency. We found small changes in the azimuthal/poloidal structure and frequency, characterized by an increase in the m-number (m_{slab}~10-13 and $\Delta m \sim 1$), along with small changes in the axial/toroidal structure ($k_{\parallel,curvature} < k_{\parallel,slab}$) and frequency ($\omega_{curvatue} < \omega_{slab}$). We also present one of the first experimental scaling of ETG mode amplitude as a function of curvature. Our key finding was a that overall levels of saturated ETG mode amplitude had a modest increase (~1.5x) which is slightly larger than existing theory and

simulations would predict, and that the power density and amplitude of individual mode peaks can increase more dramatically (~2-3x amplitude).

The second part of this thesis studies the radial transport for saturated ETG modes in CLM. ETG modes are believed to be a significant source of anomalous electron energy transport in plasmas, and a better understanding of these modes and the transport they drive across magnetic field lines is of particular interest for advanced tokamaks and future fusion reactors, where these is a continued push for energy efficiency. A specially designed triple probe has been developed, which can measure fluctuations in temperature and potential simultaneously, with a high frequency and special resolution suitable for ETG studies. We present an experimental scaling of radial transport as a function of magnetic field curvature, again one of the first of its kind. Our findings indicate a modest increase in radial transport (~2x) with increased curvature, but unlike saturated mode amplitudes, we find that radial transport saturates for higher levels of curvature in CLM.

Table of Contents

List of Figures:

List of Tables:

Acknowledgements:

First and foremost I would like to thank my advisor Prof. Amiya Sen for the opportunity to work on the Columbia Linear Machine. Special thanks are also due to Dr. Vladimir Sokolov for his continued guidance and assistance. He has been a mentor, teacher and friend, and without his tireless work and experimental expertise none of this would have been possible.

I also need to thank Prof. Stephen Sabbagh, and Dr. Jack Berkery, who provided me an opportunity to work as part of the Princeton Plasma Physics Laboratory. Although my work at Princeton is a little far from the research presented in this thesis, it was an incredible learning experience, and provided me with a strong understanding of tokamaks and a broader context for my current work.

Support for this work has been tumultuous at best, but without the generosity of the US department of energy, the national science foundation and the electrical engineering department of Columbia University none of this would have been possible. I've been a proud member of the electrical engineering department for over 9 years, and in many ways this thesis is the culmination of nearly a decade of work.

A close friend of my once told me that "it takes a village to write a thesis," and in my case it really couldn't be more true. I am indebted to the entire electrical engineering and applied physics departments, and to dozens of faculty who have served as my teachers, mentors and role-models. I am also indebted the administrative staff, who have all been tireless advocates and a constant source of support and assistance. I also need to thank the Columbia plasma lab staff assistants Jim Andrello and Nick Rivera for helping with countless small projects and coming up with common sense solutions to convoluted problems.

Finally I would also like to give very special thanks to my mother, Barbara Deck, for her continued support over the years, and to Katherine Besch-Hart for her love and patience. As for the other innumerable people who have helped me throughout this journey, thank you all so much for your love and care.

This thesis is dedicated to my father

Chapter 1

Electron Temperature Gradient Modes and Transport

1.1) Introduction

This thesis is organized into five chapters. In chapter one we give a broad overview of drift wave turbulence in general, electron temperature gradient (ETG) modes in particular, and discuss the theoretical background and some of the relevant experimental and numerical results to give context for the current experiment. The current work in many ways builds off of prior slab-ETG studies in the Columbia Linear Machine (CLM), and towards the end of the chapter we include a brief review of recent ETG work in CLM to provide additional background. For those already familiar with drift wave turbulence and ETG, it may be sufficient to read the section on prior work in CLM and skim the theoretical overview.

In the second chapter we discuss CLM as a physics device. Although extensive research is done to predict transport levels and confinement in tokamaks, tokamaks are not particularly well suited to study basic physics, hence the need for machines like CLM. We give a broad overview of the experimental operation of CLM, the probe diagnostics used, and an overview of some of the signal processing techniques that are employed for these studies. We also explain modifications made to CLM that adapt it for mixed slab-toroidal studies. Additional details of the exact diagnostics and techniques used may be elaborated on further in later sections, but this is where we will provide a broad overview of CLM's capabilities.

In the third chapter we present our results on saturated mode parameter scaling as a function of magnetic field curvature. This work focusses on characterizing changes in saturated mode amplitude and frequency, and possible changes in mode structure and saturation physics. Due to the time scales involved and our diagnostic techniques, we observe non-linearly saturated modes in a steady state setting. Unfortunately, most well-developed theory is aimed at predicting linear growth rates and frequencies, and saturated mode amplitudes are often left to numerical calculation or simulation work. Still, theory can provide some insight into expected behavior on a broad qualitative level, and we make comparisons where appropriate.

In the fourth chapter we present our preliminary results of radial thermal transport of electrons. We discuss the experimental techniques employed, a little of the theory behind the probe diagnostics used, and present scaling as a function of the applied curvature in the machine. This is one of the first results examining the dependence of radial transport on curvature in an experimental setting, and something that CLM is uniquely suited for.

In the final chapter we provide a quick final overview of our results, and present a brief high level discussion of our results in the wider context of plasma physics beyond CLM, drawing on a combination of experiment, theory, and simulation work.

1.2) A Brief History of Electron Temperature Gradient Modes and Transport in Tokamaks

Plasma turbulence plays an important role in redistributing particles and energy in a broad range of atrophysical, processing and laboratory plasmas. [1,2,3]. Plasma turbulence is also suspected of being the source of anomalous transport in magnetically confined fusion device.

Electrically charged ions and electrons that make up plasma can become trapped by magnetic field lines. Particles can move easily along the field lines, and in the absence of external forces or collisions individual particles will be confined in gyro-orbits. "Classical diffusion" across the magnetic field lines arises from collisions between particles of different species, with a step size given by the Larmor radius and time scale determined by collisionality $D \sim \nu_{ei} \langle \rho_{T_e}^2 \rangle \left(1 + \frac{T_i}{T_e}\right) \propto \frac{1}{B^2 T_e^{1/2}}$, and a similar "neo-classical diffusion coefficient" can be written for tokamaks taking banana orbits into effect. Unfortunately, diffusion in a real plasma is several orders of magnitude higher, and plasma collective effects and micro-turbulence increase diffusion substantially at higher temperatures. The difference between classical and neo-classical diffusion coefficients based on collisions and real observations is deemed "anomalous transport". To characterize this a number of experimental scalings such as "Bohm" diffusion from early experiments in the 1940's and 1950's $D_{Bohm} \sim \frac{1}{16} \frac{k_B T}{eB} \propto T/B$ and gyro-bohm scalings found in advanced tokamaks $D_{GB} \sim \rho^2 \, v_T / L_n \propto T^{3/2}/B^2$ are used, but the underlying physics driving transport can be unclear.

Ion anomalous transport driven by the interaction between ion temperature gradient modes (ITG) and Zonal Flows (ZF) are relatively well understood, but the source of electron transport is still an open issue [4]. Particularly the role of electron temperature gradient (ETG) modes in anomalous transport has been contentious as best, and it is an open question whether or not ETG fluctuations will pose a serious problem for fusion reactors. The current understanding of ETG turbulence is that the levels of fluctuation depend on a subtle mix of curvature, gradients and $E \times B$ shearing, but experimental work addressing the issue is still scant.

ETG modes have been an active area of research since the late 1980's, and theoretical and numerical ETG studies have long established the overall behavior in the linear and nonlinear limits

[5,6,7], but the transport consequences are still debatable [7,8,9] and have been an open issue for theoreticians and experimentalists alike.

Early simulations by Jenko and Dorland in 2000 [7,10] using gyrokinetic simulations found that saturated ETG transport levels fall into one of two regimes, either high or low transport. In the low-transport regime diffusion was similar to prior sheared-slab ETG simulations with transport on the order of Gyro-Bohm scaling $X_e \sim D^{ETG} \sim \rho_e^2 v_{te}/L_n \propto T_e^{3/2}/B^2$. In this case the saturation levels were determined by coupling into zonal flows. For particle species following Gyro-Bohm scaling we have:

$$\chi_\alpha \sim \frac{\rho_\alpha^2 v_\alpha}{L_{T_\alpha}} \propto \frac{T_e^{3/2}}{B^2}$$

Although this is still orders of magnitude higher than classical/neo-classical transport, the diffusion due to ETG modes would be significantly less than that of ITG modes $\chi_i \sim 60\chi_e$. This type of comparison is further reinforced by the fact that the linear equations for ETG and ITG are nearly identical, with only the species labels flipped around.

The problem is that the ETG/ITG isomorphism is broken in the non-linear and saturated regimes, and the same simulations found that under appropriate levels of shearing and temperature gradients the transport would balloon to orders of magnitude larger, on the order of ion-scale diffusivities. These results were qualified by Jenko and Dorland by performing a series of simulations all along the $\hat{s} - \alpha$ plane, where $\hat{s}$ represents the level of shearing and α represents the normalized pressure gradient within a toroidal geometry.

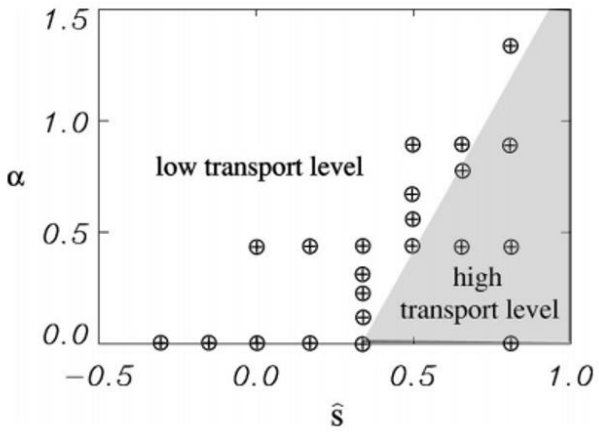

Figure 1.1: Qualitative Behavior of Transport Levels in $\hat{s} - \alpha$ space as observed by numerical simulation with $q = 1.4$, $\frac{L_{T_e}}{R} = 0.15$ and $\tau \equiv \frac{T_e}{T_i} = 1$. Reproduced from [10]

In the "high transport" regime, they found that ETG modes would saturate by coupling into radially elongated "streamers" that allowed transport up and down the temperature gradient and across the magnetic field lines. This would lead to high levels of transport despite their short wavelength. The transition between these two transport regimes was sharp and sudden, and although advanced tokamaks would operate in a parameter space predicted to have low transport levels ($\hat{s}$ small or negative and α large), it was clear that under the right conditions ETG could become a serious problem for confinement, and ETG could arguably explain high levels of observed electron heat flux.

Since then several simulations have tried to corroborate these results, and many have shown that ETG turbulence can drive transport levels much higher than simple linear predictions or Gyro-Bohm mixing length arguments would predict [7,11,12]. But other simulation results found that the formation of radial streamers could be destroyed by ion-scale turbulence, lowering ETG transport [13] or that coupling into radial streamers alone wouldn't necessarily indicate large

electron thermal transport driven by ETG [14]. Results from global fluid simulations in particular tend to predict much smaller heat fluxes.

Later work by T. Gorler and F. Jenko in 2008 [18] tried to address some of the issues in earlier simulations by invoking multi-scale analysis, and found that the combination of ETG and trapped electron (TEM) modes and ITG could still drive high transport levels. They also identified significant interactions between small scale ETG and larger ion-scale turbulence. But within the past few years, the simulation community has continued to debate the role of ETG [19], and it remains a hot button issue.

Because of the high frequency and short wavelength of ETG, evidence for its existence in tokamaks was uncertain for a number of years [15], despite the ongoing debate in the simulation and theory community. One of the earlier experimental findings were results in the DIII-D tokamak in 2006 showing that a combination of broad TEM/ETG-scale fluctuations are significantly reduced in H-mode [16]. This suggested that these fluctuations can contribute to L-mode electron heat transport, and corroborating the results of Jenko and Dorland in 2000. Later results from NSTX in 2008 experiments found ETG-like turbulence, but the turbulence was localized away from the maximum of the gradient drive L_{T_e} [17], which theory would normally predict to be a key signature of ETG turbulence.

Only in recent years have machines been able to explore ETG and ETG-like turbulence more fully. Notably, one of the first experimental observations of ETG was done at Columbia in the Columbia Linear Machine (CLM) in 2010 by Wei. et. al [20]. With numerical validation coming a couple years later from X.R. Fu et. al. [21] using the "Gyrokinetic Toroidal Code" (GTC) gyrokinetic code [22].

Similar results observing possible ETG turbulence experimentally have also been seen in the Large Plasma Device (LAPD) at UCLA [23,24] that found turbulence with $k_\perp \rho_e \sim .1$ and broad range of frequencies that followed a power law distribution $v \sim 1 - 80kHz$. Observations of ETG turbulence and coupling between high and low frequency components was also seen by Moon et. al. [25] in the $Q_T - Upgrade$ machine at Tohoku University, a modified Q-machine with similar geometry to CLM. The work by Moon found coupling between high frequency ~0.4 MHz fluctuations excited by ETG with low frequency drift waves in the ~7kHz regime.

Although they have been careful to characterize their observations as "Critical Gradient Threshold for Electron Temperature Fluctuations" and mixed TEM-ETG rather than ETG directly, observations have also recently been made in 2013 by Hillesheim et. al. in the DIII-D tokamak [26,27] and validated with numerical simulation performed in tandem [28]. They found that there was enhanced levels of fluctuation and transport once heating passed some critical threshold $L_{T_e,crit}^{-1} \sim 2.8m^{-1}$.

Despite this preponderance of recent research, there are clearly many questions to be answered, and there is still a role to be played by basic plasma physics experiments. The exact interplay of curvature, gradients, $E \times B$ shearing, and multiple species are still largely unanswered, and the experimental work has been scant. Although solving all of these problems is beyond the scope of this thesis, the current experiments being done in CLM attempt to address the importance of curvature in saturated ETG modes, and tie together observations from the slab regime with results from a mixed slab-toroidal regime, with the curvature of the magnetic field lines playing an important role in the saturated mode behavior.

1.3) Prior Work in CLM

The present research into electron temperature gradient modes is largely an extension of prior work. Electron temperature gradient modes have been studied in the Columbia Linear Machine for quite some time, but we will use this section to mention a few publications of note. ETG modes production and identification was first done by Wei et. al. in CLM in 2010 [20]. CLM was modified to generate well controlled profiles and temperature and density by using two part acceleration/heating meshes, and a new set of diagnostics were developed for working with the fast lab-frame frequencies and small spatial scales of the mode. Identification was done by measuring the frequency, the radial structure of the mode, and observing its scaling with the ETG curvature drive $\eta_e \sim L_{T_e}$. The resulting slab ETG mode with a Doppler shifted lab-frame frequency ~2-2.5 MHz, m-number 13-15, and the key scalings with gradient drive, and $\frac{\omega}{k_\parallel} \sim v_{the}$ were compared to the slab dispersion relation developed by Lee et. al. [34] and found generally good agreement. The radial transport due to the ETG mode was also explored and the findings published in [37] and experimental measurements of the electron thermal conductivity $\chi_{\perp_e} \sim 2 - 10\, m^2/s$ were found to be on the order of several gyrobohm diffusion cofficients, and to agree roughly with gyrokinetic simulation results for tokamaks.

Later numerical validation of the experiment was done by X.R. Fu et al [22] using the "Gyrokinetic Toroidal Code" (GTC) gyrokinetic code [23]. The code itself has a long history, and was developed by "Center for Gyrokinetic Particle Simulation for Turbulent Transport in Burning Plasmas", a collaboration of PPPL, Columbia University, University of Colorado, University of Tennessee, and the University of California schools. The Global Toroidal Code (GTC) is a particle in cell (PIC) simulation code optimized for large scale parallel computing and complimented by the global electromagenetic flux tube code (GEM).

The results showed that there was a wide range of modes created in the $100 - 500kHz$ range in the plasma frame, and $k_\perp \rho_e \sim 0.5$ for the fastest growing modes. However, the dominant oscillations in steady state ($t > 40\mu s$) had much longer wavelengths than the linear theory would predict and the radial structure cascaded from higher to lower m-number. The results were compared with the toroidal dispersion relation of [35] with modifications made to approximate a slab geometry and found approximate agreement.

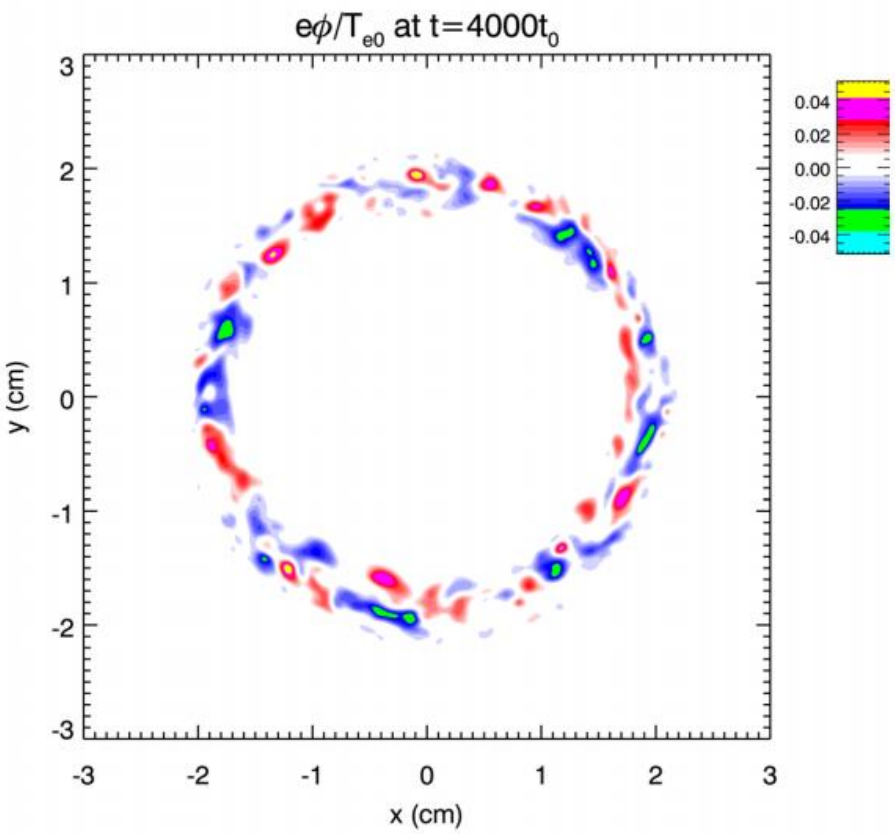

Figure 1.2: Azimuthal wave-structure of potential fluctuations for saturated steady-state ETG modes in CLM. Reproduced from Ref. [21]

Figure 1.2 shows the result of validation simulations performed by X. Fu and the Horton simulation group at UT Austin [21]. The figure shows a dominant $m \approx 12$ azimuthally and $n = 1$

along the machine axis in steady state for $t > 40\mu s$, although the steady state can be characterized as a spectrum of modes from m~10-15, $\omega \sim 0.3 - 0.5\ MHz$ in the plasma frame, $k_{\|} \sim .01\ cm^{-1}$, and about 5% oscillations.

The validation work briefly examined the fluctuation dependence on parallel wavenumber by varying the major radius of the simulation, running the original simulations at $R_0 = 300cm$ and then changing it to $R_0 = 100cm$. They found that the fastest growing mode had $n = 1$ rather than $n = 2$, and the saturated steady state was dominated by an $m = 15$ mode. Although it was only a brief piece of their simulation, it is of particular importance to our current work since changes in the major radius in a tokamak are analogous to changes in curvature levels in a linear machine, with the radius of curvature being analogous to the major radius $R_0 \sim R_c$. Overall it was shown that simulation results had a rough agreement with the experimental slab results from Wei [20], although the linear dispersion relations had significant short-comings in predicting saturated mode levels and behavior. The simulation was also unable to resolve low-*m* mode numbers m<10 where plasma response functions involve ion drift wave dynamics and acoustic modes. The authors also speculated that a more complete simulation would further damp high- *m* behavior.

The final work of interest for CLM was done by Tokluoglu et. al. [38] examining the saturation mechanisms for ETG modes. Through use of bicoherence evidence was found of coupling between high frequency modes ETG modes identified by Wei [20] at ~2.4MHz and low frequency modes in the ~50-100kHz range that were consistent with ion acoustic modes in CLM. Similar coupling between high and low frequency modes was found by Moon et. al. [25]. They used bicoherence techniques to find evidence of coupling between high frequency ETG and low frequency drift modes, and increasingly simulation work finds that low-frequency and long wavelength ion-scale behavior has a significant impact on ETG saturation. Both of these results

indicate that at least in slab regimes there is a justification for simulations containing both high frequency short wavelength electron dynamics and low frequency long wavelength ion dynamics.

1.4) A Background on Dispersion Relations and Theory of Drift Waves

In the past decade most analytical work has been over-taken by numerical simulations based on first-principle calculations, but a great deal of the underlying physics can still be understood by examining the analytical dispersion relations. An extensive review of the theory behind drift wave turbulence was completed by Horton in 1999 [29], and a similarly complete review of notable experimental work was compiled in 2009 by Tynan [30]. There have been developments since then, but these provide a good starting point for studying drift wave turbulence. It is worth pointing out that the substantial simulation work done to predict the behavior of specific types of drift wave turbulence is largely focused on the saturated limit, and most analytical theories are better suited to identify linear growth rates. Unless otherwise noted the following discussion of the basic theory is largely adapted from a combination of Horton [29] and Tynan [30], and the textbooks by Styx [31] and Goldston and Rutherford [32].

1.4.1) Diamagnetic Drifts

There are a few ways to conceptualize drift waves, but they are always inherently tied to the diamagnetic drifts currents that will appear naturally inside a plasma in the presence of local perturbations in pressure. From basic plasma theory we know that forces inside of plasma result in drifts across magnetic field lines of the type $v_F = \frac{\boldsymbol{F}\times\boldsymbol{B}}{q|B|^2}$ for a generalized force $\boldsymbol{F}$. Because of the

sign of q, this in turn will result in a charge separation between electrons and ions and result in a an $\boldsymbol{E} \times \boldsymbol{B}$ drift $v_E = \frac{\boldsymbol{E}\times\boldsymbol{B}}{|B|^2}$ that will move the plasma in the direction of the initial force. As a quick note, the scaling of v_E with **E** and **B** is unambiguous, but depending on the units being used there may be an additional coefficient, Gaussian units are common in plasma physics, and it will occasionally be written as $v_E = \frac{c\boldsymbol{E}\times\boldsymbol{B}}{|B|^2}$.

For the special case where the driving force is a pressure gradient, we can replace $\boldsymbol{F}$ with the pressure gradient divided by the plasma density to obtain

$$v_{da} = \left(\frac{1}{q_a n_a B}\right)\left(\frac{\partial p_a}{\partial r}\right)$$

For a species *a*, *p*, *n* and *q* denote pressure, density and electrical charge respectively and *B* is the magnetic field. If we have peaks and valleys of density and temperature azimuthally at some fixed radius *r*, these pressure-fronts can be represented by a wave-number $k_\perp = m/r$, and the structure will become an azimuthally rotating wave with the diamagnetic drift frequency given by:

$$\omega_{Te}^{*} = \frac{k_\perp T_e}{eBL_{T_e}} \tag{1}$$

The subscript "*e*" in Eq. (1) gives the diamagnetic drift frequency for an electron drift mode. We note that the pressure gradient has been replaced by the electron temperature gradient scale length $L_{Te}^{-1} = \frac{1}{T_e}\frac{\partial T_e}{\partial r}$. We note that the gradient in pressure can be broken down into the temperature and density components $\frac{\partial p}{\partial r} \sim \frac{\partial nT}{\partial r} \sim T\frac{\partial n}{\partial r} + n\frac{\partial T}{\partial r} \approx nT(L_{ne}^{-1} + L_{Te}^{-1})$. L_{ne}^{-1} is defined similarly to L_{Te}^{-1}, and depeding on the instability being studied the subscripts can be easily shuffled around.

1.4.2) Drift Waves as a Source of Transport

Although it would be intuitive to assume that pressure gradients across field-lines will lead to particle and thermal fluxes across field lines, the actual mechanism is somewhat non-trivial. Consider a local excess of positive charge in a magnetized plasma, for dynamics that change slowly compared to the electron thermal velocity along the magnetic field lines $\omega/k_{\parallel} \ll v_{T_e} = \left(\frac{T_e}{m_e}\right)^{1/2}$, electrons will move quickly along the magnetic field lines to neutralize the excess charge and ultimately establish a local Boltzmann density distribution $\tilde{n}_e/n_0 \approx \exp(\frac{e\tilde{\phi}}{k_B T_e})$ where k_B is the Boltzmann contant, T_e is the electron temperature, n_0 is the background density in the absence of the perturbation and $\tilde{\phi}$ is the electrostatic potential caused by the imbalance in charge. In the absence of any kind of dissipation, the plasma potential fluctuations $\tilde{\phi}$ will closely follow the density fluctuations $\tilde{n}$, and there will be minimal phase lag between them. In the parlance of drift wave turbulence this is called the "adiabatic limit."

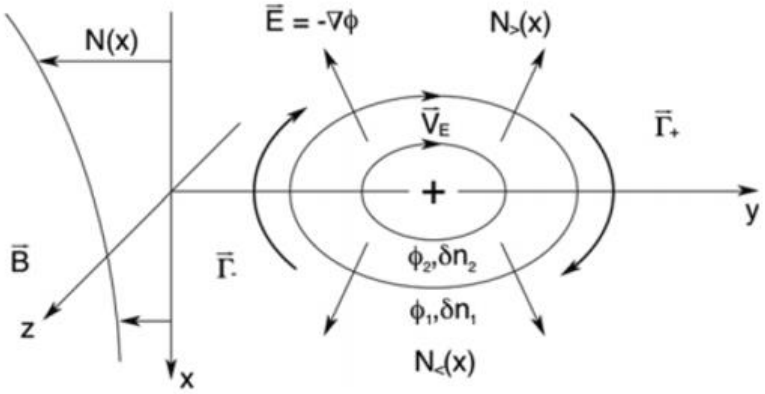

Figure 1.3: $\boldsymbol{E} \times \boldsymbol{B}$ and direction conventions for a small excess of positive-ion density. The background density gradient is in $\hat{x}$, the $\boldsymbol{B}$ field is aligned with $\hat{z}$, and $\hat{y}$ is a direction of symmetry. Reproduced from [29]

In the adiabatic limit the resulting electric field can still give rise to an $\boldsymbol{E} \times \boldsymbol{B}$ drift $v_E = \frac{\boldsymbol{E}\times\boldsymbol{B}}{|\boldsymbol{B}|^2}$. But there will be no time-averaged cross-field fluxes. In this case the fluctuation can be convected in the diamagnetic drift direction, but they will not grow. To understand this, we appeal to a simplified version of the argument presented by Tynan [30]. Time averaged fluxes in particles $\tilde{\Gamma}$, momentum $\tilde{\mu}$ and heat $\tilde{Q}$ can be expressed by the cross-correlation between fluctuations in density, velocity and temperature. For example, the time averaged heat flux can be defined as:

$$\tilde{Q} \equiv \frac{5}{2}\bar{n}\bar{T}\left[\frac{1}{\bar{T}}\left(-\frac{\langle\tilde{T}\nabla\tilde{\phi}\rangle \times \boldsymbol{B}}{B^2} + \langle\tilde{T}\tilde{\mathrm{v}}_{\parallel}\rangle\hat{b}_0\right) + \frac{1}{\bar{n}}\left(-\frac{\langle\tilde{n}\nabla\tilde{\phi}\rangle \times \boldsymbol{B}}{B^2} + \langle\tilde{n}\tilde{\mathrm{v}}_{\parallel}\rangle\hat{b}_0\right)\right] \qquad (2)$$

Where the brackets $\langle\cdots\rangle$ denote time averaging, or cross-correlation in the case of Fourier components. For us the relevant fluxes would be radial fluxes due to the $\langle\tilde{T}\nabla\tilde{\phi}\rangle \times \boldsymbol{B}$ term. Specifically, we are interested in the azimuthal component of $\langle\tilde{T}\nabla\tilde{\phi}\rangle$. For sinusoidal fluctuations without a phase lag of the type $\tilde{T} = A\tilde{\phi} \sim f(r)e^{i(m\theta + k_{\parallel}z - \omega t)}$ for some arbitrary real constant A and some arbitrary function of radius $f(r)$ we have that $\langle\tilde{T}\nabla\tilde{\phi}\rangle \cdot \hat{\theta} = Re\,\langle\tilde{T}\left(\frac{1}{r}\right)\left(\frac{\partial\tilde{\phi}}{\partial\theta}\right)\rangle = Re\,\langle iA\left(\frac{m}{r}\right)\tilde{\phi}\tilde{\phi}\rangle = 0$. We note that $\langle\tilde{\phi}\tilde{\phi}\rangle$ would normally give a real-valued auto correlation, that the coefficient $A\left(\frac{m}{r}\right)$ is purely real and that $Re\,\langle iA\left(\frac{m}{r}\right)\tilde{\phi}\tilde{\phi}\rangle$ is asking for the real component of a purely imaginary object. Similar arguments can be made about fluctuations in density and the $\langle\tilde{n}\nabla\tilde{\phi}\rangle \times \boldsymbol{B}$ term.

If there is some type of dissipation of the electron motion along the magnetic field lines, either due to collisions, wave-particle interactions, trapping etc. the resulting potential perturbations are phase shifted relative to the density perturbations $\tilde{n}_e/n_0 \approx \exp(\frac{e\tilde{\phi}}{k_B T_e})(1 + i\delta_k)$. The size of the phase difference is on the order of $\delta_k \sim (\frac{\omega \upsilon_e}{k_\parallel^2 v_{T_e}^2})$ for a collisional regime given a collisionality υ_e, or collisionless regimes can have $\delta_{k,\omega}$ determined by either electron viscosity or parallel thermal fluxes. In practice the exact form of the closure used depends on the specifics of the problem, i.e. collisional, collisionless, trapped electrons in toroidal or mirror geometry etc., but the resulting mode growth is universal.

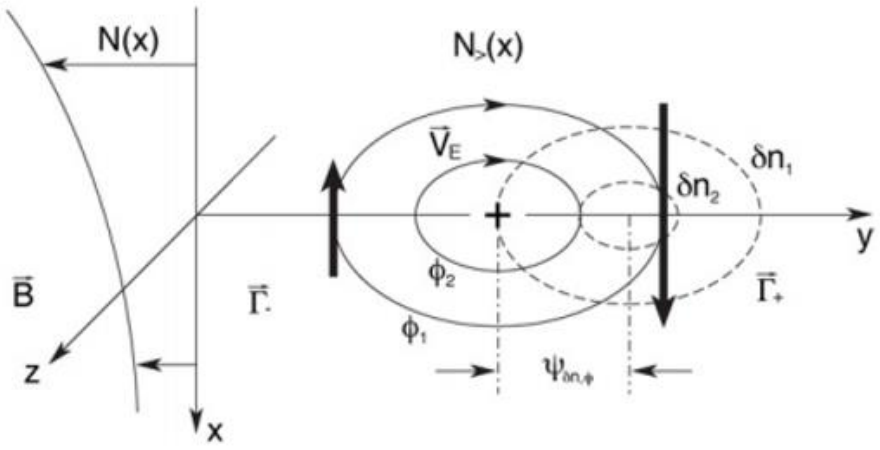

Figure 1.4: $\boldsymbol{E} \times \boldsymbol{B}$ and direction conventions for a small excess of positive-ion density with a phase lag between the density and potential fluctuations. The background density gradient is in $\hat{x}$, the $\boldsymbol{B}$ field is aligned with $\hat{z}$, and $\hat{y}$ is a direction of symmetry. Reproduced from [29]

In the above figure we see the result of a phase lag $\Psi_{\omega,k}$ between the density and potential fluctuations. The disturbance will propagate along the axis of symmetry with the density fluctuations leading the potential fluctuations. Given the clockwise motion, more particles are brought to the right from the top and fewer particles are brought to the left from the bottom. This

leads to a net flux of particles along the direction of the gradient, and causes the disturbance to be self-reinforcing and grow exponentially as $e^{\gamma_k t}$ where $\gamma_k/\omega_k \propto \delta_k$. Again, arguments based on the correlation between fluctuations in density, velocity and temperature can be used to also show that the delayed response of the potential fluctuations will cause net transport along the pressure gradient. Drift waves that grow large enough can interact non-linearly with perturbations at other wavenumbers and special scales. If these other perturbations are damped, this can act as a source of dissipation for the system. The interaction of all these different modes will create a wide spectrum of instabilities, and is sometimes dubbed "drift wave turbulence."

Drift waves encompass an incredibly broad spectrum of instabilities, and before delving into the specific of electron temperature gradient driven modes we will summarize by pointing out a few key signatures that set drift waves apart from other types of turbulence including:

- Drift waves are electrostatic, and normally have $E = -\nabla\phi$ where ϕ is the scalar potential.
- Drift waves are will rotate azimuthally across the magnetic field lines with a speed governed by the diamagnetic drift frequency. Combined with their fast motion across the field lines this gives them a generally helical structure with $k_\perp \gg k_\parallel$.
- The perpendicular wave structure of drift waves will be much larger than the Debye Length $k_\perp \lambda_D \ll 1$. Features larger than a Debye length are by and large electrically shielded, and as a result drift waves are quasineutral.
- We mention that for $\omega/k_\parallel \ll v_{T_e}$ drift wave modes don't drive significant transport and don't have large growth rates. Alternately, modes that have a Landau-style resonance with $\omega \sim k_\parallel * v_{phase,\parallel}$ have high levels of wave-particle interaction, and when we

examine ETG dispersion relations we will find that this resonance plays an important role in driving unstable modes.

The thermal and particle diffusion caused by drift waves depend on the gradient scale lengths involved, and we often talk about the density gradient scale length $L_n^{-1} = -\partial_x \ln N$ and a similar temperature gradient scale length $L_T^{-1} = -\partial_x \ln T$. Discussions of diffusivity are often compared to two reference diffusivities, Bohm-Diffusion and Gyro-Bohm Diffusion:

$$D_{Bohm} = \frac{cT_e}{eB} \tag{3}$$

And for drift waves we talk about Gyro-Bohm Diffusion or Drift-Wave Diffusion

$$D_{dw} = D_{GB} = \left(\frac{\rho_s}{L}\right)\left(\frac{cT_e}{eB}\right) \tag{4}$$

Depending on the reference being used there will occasionally be an additional coefficient of $1/16$ on D_{Bohm} which stems from early experimental plasma studies. In Gyro-Bohm Diffusion the factor $\left(\frac{\rho_s}{L}\right) \ll 1$, where $\rho_s = \frac{m}{|q|}\left(\frac{v_\perp}{B}\right) \propto \frac{T^{.5}}{B}$ is a Larmor Radius and L is the gradient scale length of interest. The most important difference between these two diffusivities is the scaling with temperature and magnetic field strength, $D_{Bohm} \propto \frac{T_e}{B}$ and $D_{GB} \propto \frac{T_e^{3/2}}{B^2}$. For our present work we find it most convenient to make comparisons with D_{GB}, and we point out that the scaling as $1/B^2$ is similar to classical estimates made based on collisionality.

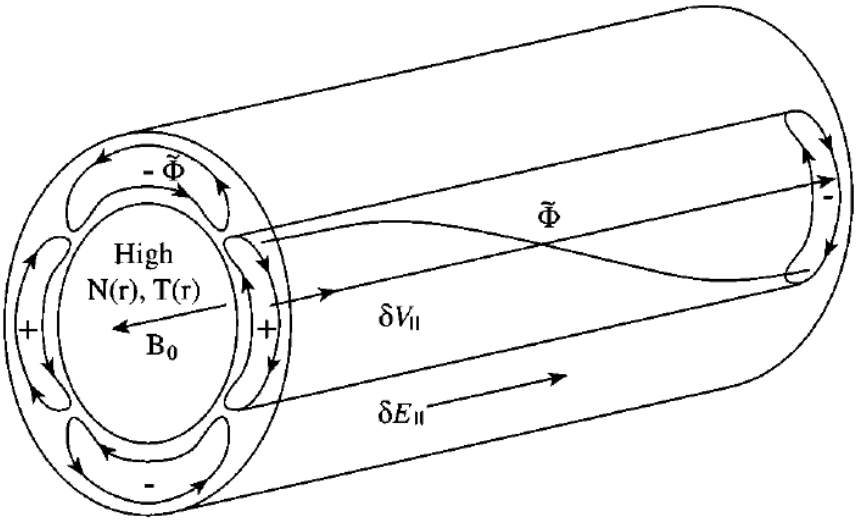

Figure 1.5: Drift Wave Motion in a Cylindrical Device, like the Columbia Linear Machine for a dominant *m*=2 mode. Reproduced from [29]

The result of drift waves in a cylindrical device like CLM are azimuthally separated pockets of positive and negative charge and density. Each of these pockets of charge will cause the plasma to cycle and churn, potentially bringing hot dense plasma from the center to the periphery.

1.4.3) Theory and Dispersion of ETG

Before we present the specifics of ETG dispersion relations, we will briefly discuss drift wave dispersion relations and the plasma dispersion function in general. Kinetic dispersion relations for drift waves can be found by starting with a Vlasov-Poisson system and using a peturbative technique the "δf" approximation. Here we assume that there is a near-maxwellian background distribution f, and a very small perturbation such that $\delta f \ll f$. Integrating out the equation in velocity space will give density fluctuations δn as a function of δf and f. Reinserting

this into the Vlasov Equation obtains a dispersion relation of the type $D(\omega)\varphi = 0$ and ω is complex valued. To find non-trivial solutions where $\varphi \neq 0$ we can look for solutions where for $D(\omega) = 0$. New or modified drift wave dispersion relations for $D(\omega, k)$ can be derived from kinetic or gyrokinetic equations, or can occasionally be approximated by fluid equations, but here we will discuss the 'vanilla' plasma dispersion function.

For drift waves we will typically have the resulting plasma dispersion function:

$$D(\omega, k) = \sum_j \left(\frac{n_j q_j^2}{T_j}\right)\left[1 - \langle \frac{\omega - \omega_{*,j}(\epsilon)}{\omega - \omega_{D_j} - k_\parallel v_\parallel} J_0^2 \rangle\right] \tag{5}$$

Where we have

$$\omega_{*j} = \frac{k_y c T_j}{e_j n_j B}\frac{dn_j}{dr}\left[1 + \eta_j(\epsilon - \frac{3}{2})\right] \tag{6}$$

and

$$\epsilon = m_j v^2 / 2T_j$$

Where we take the sum over all the particle species on interest, each one denoted by j. The brackets denote an integration over velocity-space, often with the assumption of a Maxwell Boltzman distribution $\langle A \rangle = \int d^3 v F(v) A(v)$. Here J_0 is the zero-order Bessel function resulting from gyro-averaging (phase averaging) the gyrokinetic Vlasov equation, and we have introduced a more complete version of the diamagnetic drift frequency ω_{*j} along with the magnetic curvature drift frequency $\omega_{D_j} = 2\varepsilon_n \omega_{*j}$.

Numerous dispersion relations exist for ETG modes under varying levels of curvature, all of which provide qualitatively similar results. The most complete review of the transition between

slab and toroidal ETG modes was produced by Kim and Horton [33] and was based around a kinetic dispersion relation of the type $D_k(\omega)\Phi_k = 0$ where

$$D = D_a - \int_0^\infty \int_{-\infty}^\infty \frac{\left\{\tau\omega - k_\perp\left[1+\eta\left(\frac{v^2}{2}-\frac{3}{2}\right)\right]\right\} J_0^2\left(\frac{k_\perp v_\perp}{\tau^{.5}}\right) e^{-\frac{v^2}{2}}}{\tau\omega - k_\perp\varepsilon_n\left(\frac{1}{2}v_\perp^2 + v_\parallel^2\right) - k_\parallel v_\parallel \tau^{.5}} \frac{(v_\perp dv_\perp dv_\parallel)}{(2\pi)^{.5}} \tag{7}$$

Where $D_a = 1 + 1/\tau$, $\tau = T_i/T_e$, $\varepsilon_n = L_n/R$, and the wavenumbers and frequency $k_\perp$, $k_\parallel$ and ω are normalized by $\rho_{ei} = v_{ei}/\omega_{ce}$, L_n and L_n/v_{ei} respectively where $v_{ei} = \left(\frac{T_i}{m_e}\right)^{\frac{1}{2}}$ is the thermal velocity of the electrons due to ion temperature. The dispersion relation is a little unwieldy and is typically solved for numerically, but it captures most of the expected transition behavior of the mode. Results based off of either fluid or kinetic models in the slab and toroidal limit are also readily available [34,35]

We point out two important parameters of interest which can be seen in both the ETG dispersion relation and the more general plasma dispersion function, ε_n and η_e. The parameter $\varepsilon_n = \frac{L_n}{R} = \omega_d/2\omega^* \approx \frac{L_n}{R_c}$ is known as the toroidicity, and it frequency comes up in theoretical discussions. "Toroidal" modes have a curvature in the magnetic field lines, represented by either the tokamak major radius R or the radius of curvature of the field lines R_c, and in the case where ε_n is large the ω_{D_j} term in the denominator of the integral will play an important role in determining which particles are resonant. In the case where ε_n is small the resonant particles are determined by the parallel velocity $k_\parallel v_\parallel$.

The other critical parameter of interest for stability is the gradient drive, defined as:

$$\eta_e = \left(\frac{\partial \ln T_e(r)}{\partial r}\right)\left(\frac{\partial \ln n(r)}{\partial r}\right)^{-1} \tag{8}$$

$$\eta_{etg} \approx \left(\frac{\partial \ln T_e(r)}{\partial r}\right) = L_{T_e}^{-1} \tag{9}$$

For modest levels of $\left(\frac{\partial \ln T_e(r)}{\partial r}\right)$ and $\left(\frac{\partial \ln n(r)}{\partial r}\right)^{-1}$, and in the absence of a gradient in density this is replaced by $\eta_e \approx \left(\frac{\partial \ln T_e(r)}{\partial r}\right) = L_{T_e}^{-1}$. Depending on the value of the gradient drive, the dispersion relation may or may not have solutions corresponding to unstable growing modes.

Rather than try solving the dispersion relation directly to look for unstable modes, a common practice has been to use the Nyquest Diagram Technique, which is also found in the study of control systems. The technique involves sweeping the complex-valued ω through the boundary of the entire positive half-plane and plotting out the corresponding values of $D(\omega)$ on the complex plane:

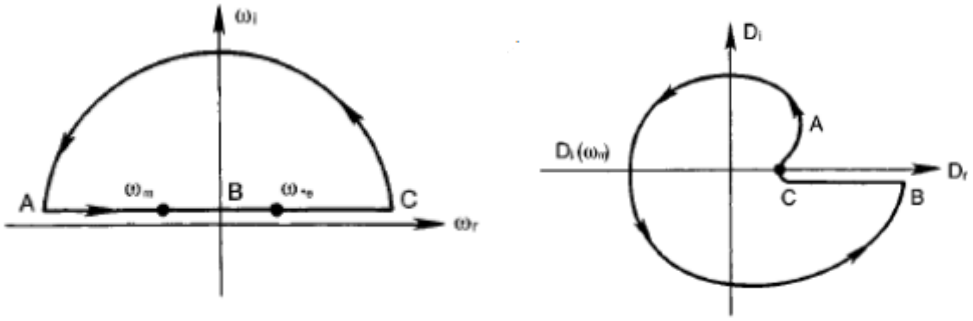

If the closed curve of $D(\omega)$ encloses the origin, there will be some solution for which $D(\omega) = 0$ and ω is contained in the positive half plane, and has a positive imaginary component representing an unstable growing mode. This technique was used to determine that there would be an unstable growing mode for a chosen set of parameters without the need to solve for the unstable mode directly. Given the basic dispersion relation early theoreticians found that there would be no growing modes for values of $\eta < 2/3$, but for $\eta > 2/3$ the Nyquest diagram would enclose the

origin and unstable modes can exist. This led to the concept that unstable growing modes could only exist if there was sufficiently large gradients such that:

$$\eta > \eta_{crit} \sim 2/3$$

Further work done has been aimed at refining the value of η_{crit} and determining the interplay between the value of η_{crit}, the toroidicity ε_n, and the resulting mode growth rates and saturated levels. The work by Kim and Horton [33] Found a series of numerical curves for the critical gradient as a function of the toroidicity and perpendicular wavenumber $\eta_{crit}(\eta, k_y)$ and found that it could be approximated as $\eta_{crit}(x) = \frac{1+x^4}{1+x^4/3}$ for $x = \frac{k_\parallel R_c}{2k_\perp \rho}$, implying that toroidal modes generally had lower values for η_{crit} and could be excited more easily.

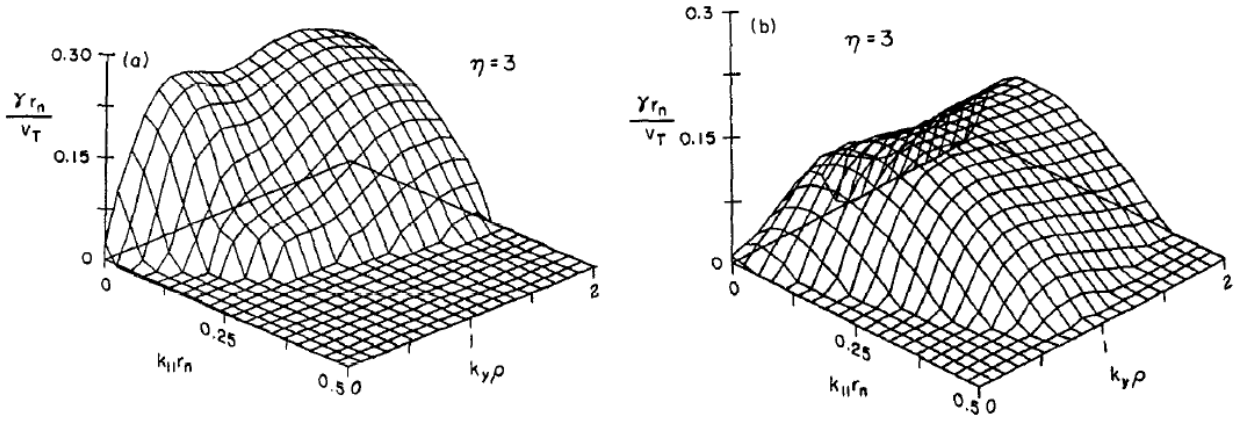

Figure 1.6: ETG/ITG growth rates as a function of the wave-number when $\eta = 3$ (a) in a toroidal regime where $\varepsilon_n = 0.1$, (b) in the slab limit where $\varepsilon_n = 0$. Reproduced from [33]

The other key result from their studies on ETG was that toroidal modes had higher linear growth rates overall, and that the maximum growth rates peaked for lower values of $k_\parallel$ compared to modes in the slab limit.

Simulation work addresses the issue of critical gradients in tokamaks from a slightly different perspective, and they talk about a normalized critical gradient with respect to the major tokamak radius, which normally takes the form of

$$\left(\frac{R}{L_{T_e}}\right)_{crit} = \max\left[A', B'\left(\frac{R}{L_n}\right)\right]$$

With coefficients typically in the range of $2.5 < A < 5$ is some general baseline and $\frac{2}{3} < B' \sim \eta_e^{crit} < 1$ [36].

Work by Jenko and Dorland [36] found that the onset of the high-transport caused by radial streamers roughly coincided with the critical gradient thresholds predicted by earlier theory. They found that toroidal ETG is destabilized by electron (grad B and curvature) drift resonance and is subject to a critical value of R/L_{T_e} while slab-like ETG is driven by electron transit resonance and is subject to a critical $\frac{L_s}{L_{T_e}}$ where L_s is the shear length for flat profiles of density and a full model for the critical gradient threshold was expressed as

$$\left(\frac{R}{L_{T_e}}\right)_{crit} = \max\left[(1+\tau)\left(1.33 + \frac{1.91s}{q}\right)(1 - 1.5\epsilon) \times \left[1 + 0.3\epsilon\left(\frac{dk}{d\epsilon}\right)\right], .8\left(\frac{R}{L_n}\right)\right] \qquad (10)$$

Given the above discussion, it might be assumed that higher gradient scale lengths and curvature simply lead to bigger and faster growing modes, but the need for particles to satisfy the wave resonance condition $\frac{\omega}{k_\parallel} = v_{phase,\parallel}$ complicates the situation. Generally the radial dependence of $\eta \sim L_{T_e}$ and ω_{*j} leads to mode structures that are localized around a specific radial position $r + \Delta r$, with a radial mode width normally given by $\Delta r = (\rho_s L)^{1/2}$, outside of that range and the parallel velocity of the particles may no longer be resonant with the values of ω consistent ω_{*j}.

This leads to the paradoxical observation that a sufficient gradient is needed to excite a mode, but extremely large gradients can reduce the size of the mode.

In a toroidal geometry the effect of strong shearing can also be used to break the wave-particle resonance, and the effective value of $k_{\|}$ will have a dependence on both geometry and shearing. In a torus the potential fluctuations can be expressed using eigenfunctions of the type:

$$\Phi = \Phi(r) + \sum_{m,n} \Phi_{m,n}(r) e^{im\theta - in\phi - i\omega t} + complex\ conjugate \tag{11}$$

Where m and n are the poloidal and toroidal rotation numbers associated with the mode, θ is the poloidal coordinate, ϕ is the toroidal. The magnetic field in a toroidal system takes the form $\boldsymbol{B} = B_\theta \hat{e}_\theta + B_\phi \hat{e}_\phi$ and ι or $\frac{1}{q}$ will become $\frac{1}{q(r)} = \frac{RB_\theta}{rB_\phi}$ with R being the major radius and r the minor radius of the tokamak. This will lead to the expression for magnetic shear, or the rate of change of the twist of the magnetic field lines

$$S = \frac{r}{q}\frac{dq}{dr} \tag{12}$$

The effective value of $k_{\|}$ for the toroidal geometry can be written as

$$k_{\|}^{m,n} = -ib \cdot \nabla \ln \phi_{m,n} = \frac{m - nq}{qR} \tag{13}$$

The above equation shows that $k_{\|}$ is determined by the difference between the twisted magnetic field lines and the twist of the perturbation. Since the effective value of $k_{\|}$ changes with radial location, the location of the mode resonance will change as well, resulting in radially localized modes.

Ultimately drift waves in cylindrical devices will be confined to specific radii, but the equivalent for tokamaks will be modes localized to specific magentic surfaces based on their q values, with the width of the modes determined by the shearing *s*. Typically higher levels of shear will result in quicker variations in $k_{\parallel}$ and smaller mode widths as a result of the damping. Still, the interaction of shearing with non-linearly saturated ETG modes is unable to be explained by linear theory, and it colors the debate on whether or not ETG can explain anomalous transport in advanced tokamaks.

1.5 A Simplified Fluid Model for Scaling

Rather than working with a full kinetic equation, the general physics can be better explained using a simpler fluid model for easily calculation [41]. Starting from

$$continuity: \quad \frac{\partial \tilde{n}_e}{\partial t} + v_{E\times B} \cdot \nabla n_e + n_e \nabla_{\parallel} v_{\parallel} + \frac{c}{eB} \nabla \cdot \left(\hat{b} \times \nabla \tilde{p}_e\right) = 0 \tag{14}$$

$$parallel\ momentum\ balance: \quad m_e n_e \frac{\partial v_{\parallel}}{\partial t} + \hat{b} \cdot \left(e n_e \tilde{E} + \nabla \tilde{p}_e\right) = 0 \tag{15}$$

$$adiabatic\ equation\ of\ state: \quad \frac{\partial \tilde{p}_e}{\partial t} + v_{E\times B} \cdot \nabla p_e + \frac{5}{3} p_e \nabla_{\parallel} v_{\parallel} = 0 \tag{16}$$

Which are the continuity equation, the parallel momentum balance, and the adiabatic equation of state respectively. The equation of state ignores FLR heat loss and for simplicity we assume $T_e = T_i$, adiabatic ion response, electrostatic modes $\tilde{E} = -\nabla\tilde{\phi}$ and quasineutrality $\tilde{n}_i = \tilde{n}_e$. This heavily simplified equation will understate the effect of curvature slightly, and it will overstate the growth

rate for higher values of $k_{\parallel}$, but it can still be used to illustrate some of the qualitative expectations. Combining the above we can create a general expression for mode frequency and growth rate:

$$1+\left(\frac{\omega_e^*}{\omega}\right)\left(\frac{1}{\eta_e}\right)+\frac{\omega_{de}}{\omega}\left(\frac{\omega_e^*}{\omega}\left(1-\frac{2}{3\eta_e}\right)-\frac{5}{3}\right)+\left(\frac{k_{\parallel}v_{t,e}}{\omega}\right)^2\left(\frac{\omega_e^*}{\omega}\left(1-\frac{2}{3\eta_e}\right)-\frac{8}{3}\right)=0 \qquad (17)$$

Where we have $\omega_e^*=\frac{k_\theta KT_i}{eBL_T}$, $L_T=-(\frac{d\ln(T_e)}{d\ln(r)})$, $\omega_{de}=\frac{2\omega_e^*L_T}{R_C}=2\omega_e^*\varepsilon_n$, R_c is the magnetic curvature radius and the electron thermal velocity is given by $v_{t,e}=\sqrt{\frac{T_i}{m_e}}$ Rearranging slightly we can write this as an explicitly as a cubic function for ω/ω^*

$$\left(\frac{\omega}{\omega_e^*}\right)^3+\left(\frac{\omega}{\omega_e^*}\right)^2\left(\frac{1}{\eta_e}-\frac{5}{3}(2\varepsilon_n)\right)+\left(\frac{\omega}{\omega_e^*}\right)\left((2\varepsilon_n)\left(1-\frac{2}{3\eta_e}\right)-\frac{8}{3}\left(\frac{k_{\parallel}v_{t,e}}{\omega_e^*}\right)^2\right)$$

$$+\left(\frac{k_{\parallel}v_{t,e}}{\omega_e^*}\right)^2\left(1-\frac{2}{3\eta_e}\right)=0 \qquad (18)$$

This equation has three roots, one real ($Im(\omega)=\gamma=0$) and one complex conjugate pair ($|\gamma|>0$). We take the complex root with positive imaginary component as our growing mode. From there we can determine mode frequency and growth rate as a function of toroidicity $\varepsilon_n=L_{Te}/R_c$ and normalized values of $k_{\parallel}\sim\frac{k_{\parallel}v_{t,e}}{\omega_e^*}$. For the purposes of our calculation we take $\eta_e\sim3$, which is typical for CLM parameters and satisfies $\eta_e>\eta_{e_{crit}}$ for most reasonable theories of slab or mixed-slab toroidal ETG regimes.

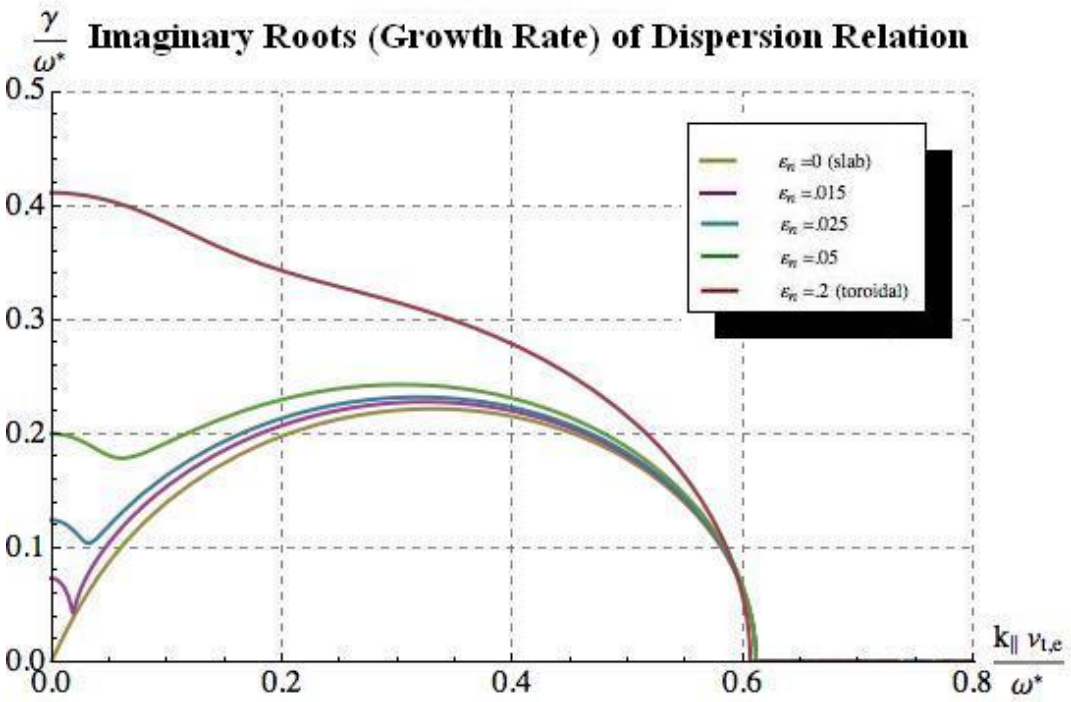
γ/ω*
Imaginary Roots (Growth Rate) of Dispersion Relation
0.5
0.4
0.3
0.2
0.1
0.0
0.0
0.2
0.4
0.6
0.8
k∥ v_t,e / ω*
ε_n =0 (slab)
ε_n =.015
ε_n =.025
ε_n =.05
ε_n =.2 (toroidal)

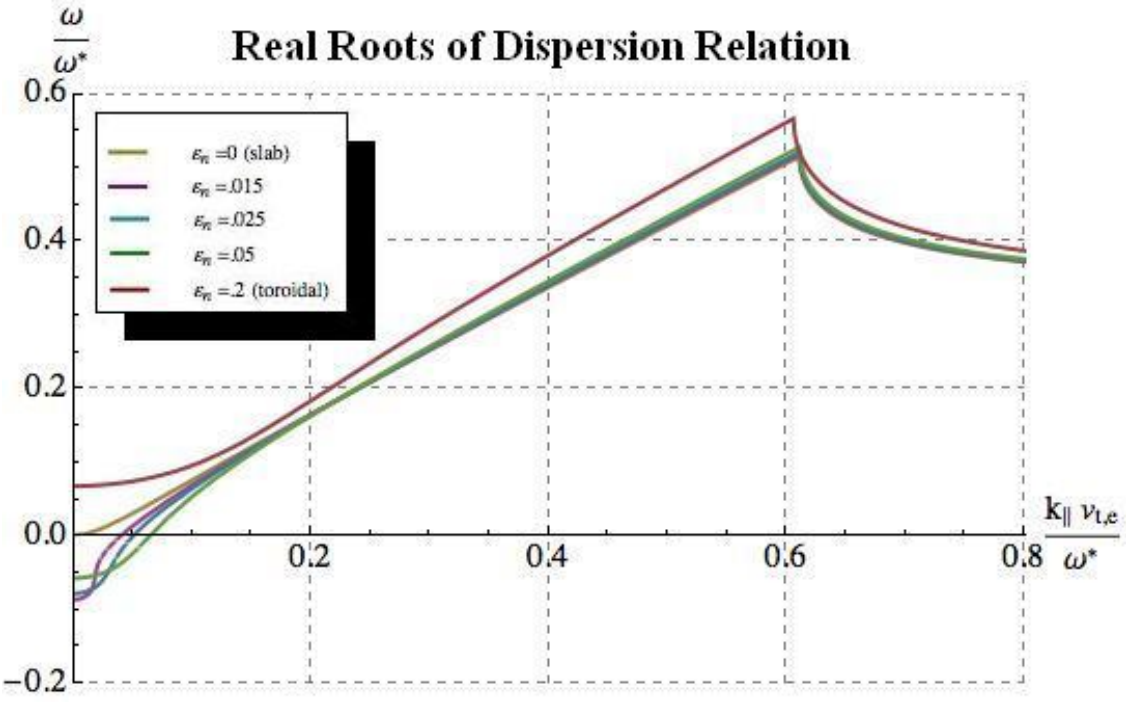
ω/ω*
Real Roots of Dispersion Relation
0.6
0.4
0.2
0.0
−0.2
0.2
0.4
0.6
0.8
k∥ v_t,e / ω*
ε_n =0 (slab)
ε_n =.015
ε_n =.025
ε_n =.05
ε_n =.2 (toroidal)

Figure 1.7: Growth Rate and Frequency of Slab-Toroidal ETG Fluid Model

In Fig. 1.7 we can see the resulting growth rate and real frequency of the mode for varying levels of $k_{\|}$ normalized as $\frac{k_{\|}v_{t,e}}{\omega_e^*}$ for a simple fluid model of ETG with changing curvature. We will point out a few of the key features that it shares in common with more complicated dispersion relations. First we note that there is a finite range of $k_{\|}$ for which the modes are growing between $\frac{k_{\|}v_{t,e}}{\omega_e^*} \sim 0 - .6$ with a maximum around .3. In this range of $k_{\|}$ values we see that the real frequency ω/ω^* also varies between ~0-.6, and scales with $\frac{k_{\|}v_{t,e}}{\omega_e^*}$ approximately linearly. This is analogous to resonant particles in the kinetic dispersion relationship, where $\omega \sim k_{\|}v_{\|}$ is required to excite ETG modes in the absence of curvature.

Aside from having the appropriate general shape and scaling of ω with k and $v_{\|}$, the behavior as a function of increased curvature also fits well with the broad results from kinetic dispersion relations. Each line on the curve was taken with a different level of curvature ε_n. Starting from the bottom of the γ plot the yellow line with $\varepsilon_n = 0$ represents a pure slab mode. As the curvature in increased the shape of the curve deforms, and the growth rate increases for smaller values of $\frac{k_{\|}v_{t,e}}{\omega_e^*}$. In the presence of extremely large curvature, represented by the red $\varepsilon_n = .2$ line, the fastest growing modes have $\frac{k_{\|}v_{t,e}}{\omega_e^*} \to 0$.

Again, this result is similar to results predicted by kinetic dispersion relations, and numerical curves from Kim [33] indicate that the fastest growing modes move to smaller values of $k_{\|}$ for higher levels of curvature, and that the overall growth rate for the fastest growing modes increases for higher levels of curvature.

For slab modes there is a wide spectrum of value for $k_{\|}$ with significant growth-rates, but the value of $k_{\|}$ with the maximum growth rate occurs around $k_{\|}{\sim}.35\omega^{*}/v_{t,e}$ and corresponds to a real frequency of $\omega{\sim}.25\omega^{*}$. For typical CLM parameters $\omega^{*}{\sim}3*2\pi MHz$ and $v_{t,e}{\sim}3.8x10^{-4}m/s$ this gives $k_{\|}{\sim}.005\,cm^{-1}$ and $\omega{\sim}750kHz$. These numbers are roughly consistent with measurements seen in the lab, roughly ~20% off, but to first order the equation is able to at least give a reasonable estimate of growth rates and real frequency. It is unphysical for CLM to operate in the region of very high curvature, and excluding the purely toroidal-ETG red curve even the fastest growing modes only have their growth rates increase by ~10% if not less.

The key predictions that we can make about increased levels of curvature can be summarized as follows:

- As curvature increases the overall growth rate of the modes and subsequent saturated amplitude is predicted to increase. This comes from both fluid and kinetic models.
- As curvature increases the resonant values of $k_{\|}$ may shift to lower values. Again this can be seen in both fluid and kinetic models.
- If $k_{\|}$ shifts to lower values, we would expect that the real frequency in the plasma frame to scale with $k_{\|}$ linearly. For reasons that will be elaborated on further, this measurement is difficult to make in CLM, but there is some evidence of shifting value in $k_{\|}$ along with reductions in real frequency.
- From kinetic theory [33] the critical gradient threshold will be reduced, $\eta_{e_{crit,toroidal}} < \eta_{e_{crit,slab}}$. We don't attempt to measure this effect, but we note that $\eta_e > \eta_{e_{crit,slab}}$ through all of our experiments.

Chapter 2

Columbia Linear Machine as a Physics Device

2.1 The Columbia Linear Machine

Studying ETG behavior directly in tokamaks has two shortcomings, both of which are easily overcome by studies in the Columbia Linear Machine (CLM). The first problem is that tokamak plasmas are inherently chaotic, and ETG is rarely an isolated behavior. The gradients that drive ETG are largest in the tokamak pedestal, and while edge localized modes (ELM) and H-mode physics in the pedestal are all active areas of research, they are typically treated as a collection of behaviors driven by the interaction between ion gradients, electron gradients, shearing effects, the effect of heating and neutral beam injections etc. The second problem is that tokamaks are often limited in what diagnostics are able to be used in the plasma. There has been some success using microwave interferometry to obtain results from tokamaks [39][40], but the combination of high frequency, small spatial wavelengths, and restrictions on invasive probe techniques and plasma facing components limits the range of possible studies.

By comparison, CLM operates in a well understood cylindrical geometry where it is possible to establish well defined gradients in both ion and electron temperature and density. This allows CLM to study ETG separate from other confounding variables and physical processes. CLM is also easily adapted to any number of probe and diagnostic techniques, including the direct use of Langmuir probes, which leads to relatively unambiguous measurements and results. These

two factors have been important for the historical success of CLM studying various types of drift wave turbulence, and are key features that allow the present research to be done.

The Columbia Linear Machine (CLM) is cylindrical linear machine that produces a steady-state, quiescent, and near-collisionless hydrogen plasma. The magnetic field produced in the machine is primarily axial, running along the length of the device, although recent modifications have been made to produce curved fields lines by including a second mirror coil inside of the device, which operates similar to a magnetic mirror trap.

CLM is well suited to produce and investigate different kinds of instabilities due to its steady state nature, and flexibility to accommodate wide variations in plasma parameters. This allows instabilities to be produced in a controlled fashion with well-defined profiles and temperature and density, and for the acquisition of large continuous data sets. Some notable past accomplishments were successfully identifying and studying ion temperature gradient (ITG) modes in a slab and mixed slab toroidal geometry [41],[42], trapped electron modes (TEM) [], and recently electron temperature gradient modes [20]. The relatively simple geometry of CLM also allows for easier comparison to fundamental theories compared to mode complicated devices, such as tokamaks and stellarators. Another feature of CLM is relatively low plasma density and particle temperature, which allows for simple and well-defined probe based diagnostic techniques, many of which are impossible in advanced tokamaks. Since CLM operates in a different temperature and density regime, a level of caution and care needs to be taken before extrapolating results from CLM to behaviors on larger scale tokamak devices, but basic plasma physics and fundamental scaling laws are typically independent of the parameter space, and are particularly well suited for CLM studies.

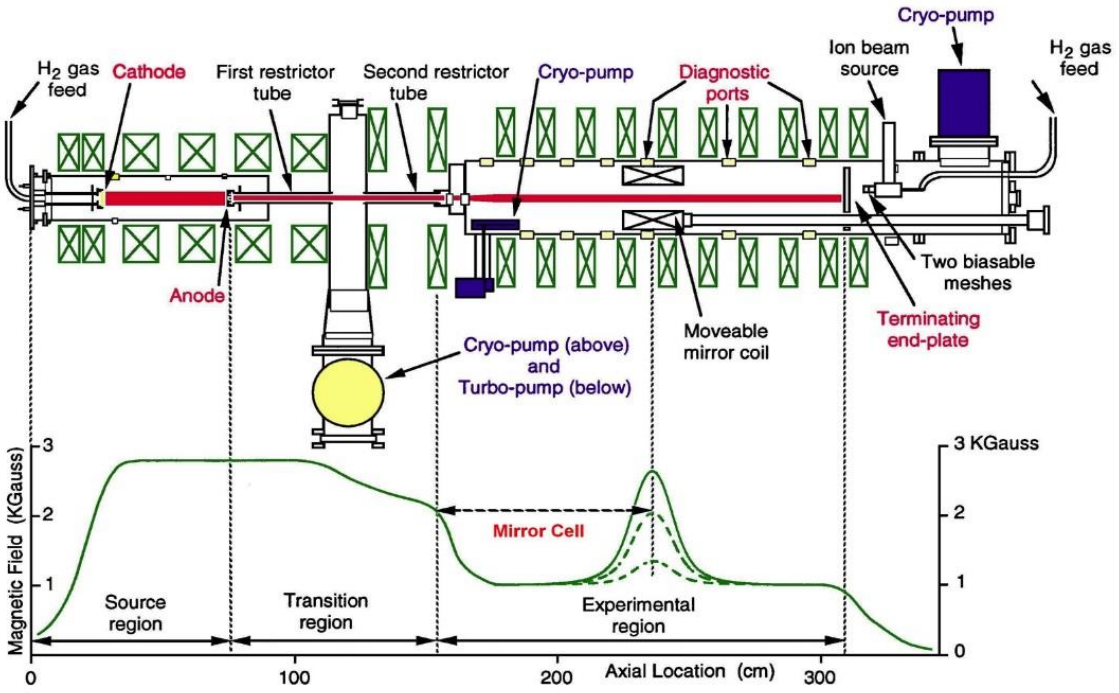

Figure 2.1: Schematic Representation of CLM

A schematic of CLM is shown in Fig 2.1, which shows the main regions within the device [44]. More detailed discussions of the magnetic field structure and the biasing schemes will be presented later on, but the figure proves a rough introduction. The machine consists of three primary regions of operation: the source region, the transition region, and the experimental region, each of which has a different magnetic field strength and background pressure due to independently controlled mirror coils and differential pumping.

Hydrogen plasma is generated in the source region by a hot tungsten cathode gas discharge. The source region is maintained at a higher background pressure ($5\text{x}10^{-4}\ Torr$)and magnetic field (~3kG) than the rest of the device, and only a small fraction of the original neutral particles are maintained in the experimental region. The plasma generated in the source region leaves through a small circular limiter anode with a radius $r = 1.8cm$ and enters the transition region.

The transition region is where the different biasing and heating meshes are located, and where profiles of temperature and density for different species can be achieved. The transition region is important because it is where thermalization occurs, and the electron and ion distributions relax to Maxwellian. The magnetic field is not uniform along the transition region, and varies between the $B = 3kG$ in the source region to the $B = 1kG$ of the experimental region. Because of the lower magnetic field strength, the plasma column also expands from radius ~1.8 cm in the source region to about radius ~3 cm in the experimental region. The transition region also houses the biasing meshes used to set the profiles of electron temperature.

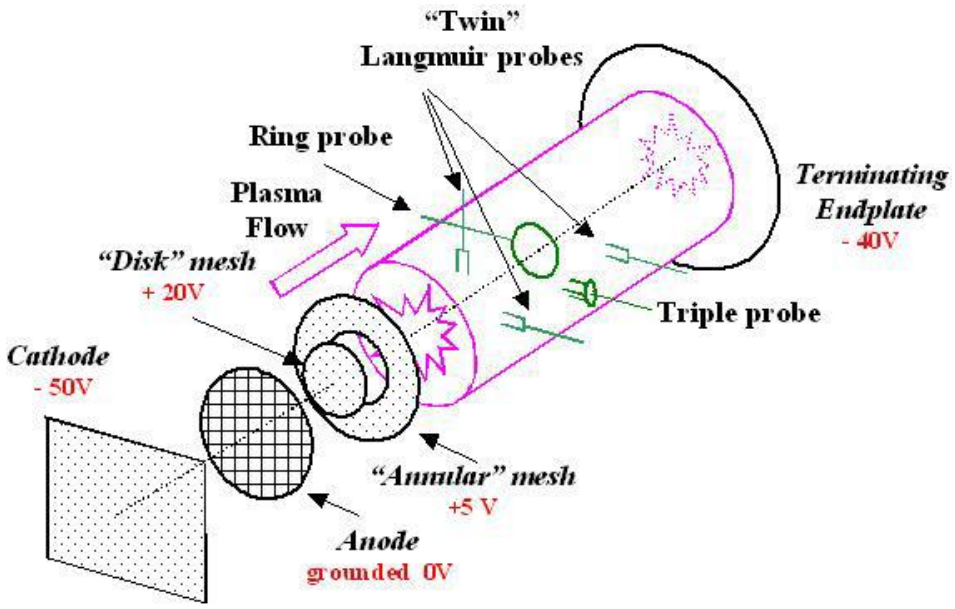

Figure 2.2: Layout of Biasing and Diagnostics in CLM

Fig. 2.2 shows a diagram of the biasing scheme used in CLM. The cathode and anode located in the source region will typically set the overall plasma density, and along with the terminating end plate have subtle impacts on the profile of plasma potential. In the transition region a circular "disk" mesh of $r{\sim}1.2cm$ and an annular "ring" mesh of $r{\sim}1.2-2.0cm$ can be adjusted to accelerate electrons as the go through the transition region. The electrons are thermaized before

entering the experimental region, and the result is a profile of electron temperature that varries with radius. Depending on the experiment being performed, the disk and ring mesh can be adjusted to manipulate the profile of temperature and the gradient drive η_e, which can be measured and verified experimentally.

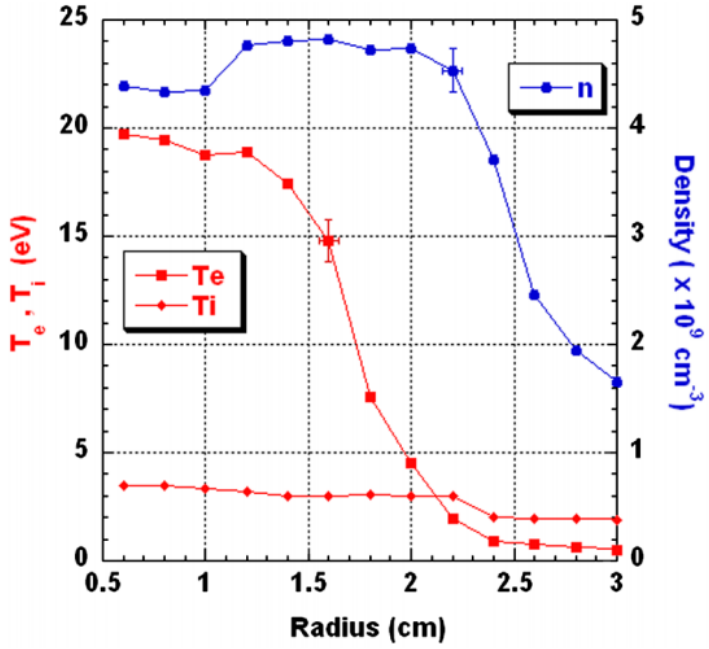

Figure 2.3: Typical Density and Temperature Profiles in CLM ETG studies

In Fig. 2.3 we show a typical density and temperature profile resulting from the heating elements. The peak of the gradient in electron temperature occurs around $r = 1.8cm$ and the gradient drive is highest around $r = 2.0\ cm$. Our experimental measurements are often taken around $r = 2.0\ cm$, well away from the roll-off in density that occurs at the periphary of the plasma for $r > 2.3\ cm$. In Fig 2.4 we show a typical floating and plasma potential profile which can be used to determine $\boldsymbol{E} \times \boldsymbol{B}$ rotation. Typically this will be in the range of $125 - 175kHz$ depending on plasma paramaters, but in practice it is more convenient to measure the rotation frequency experimentally.

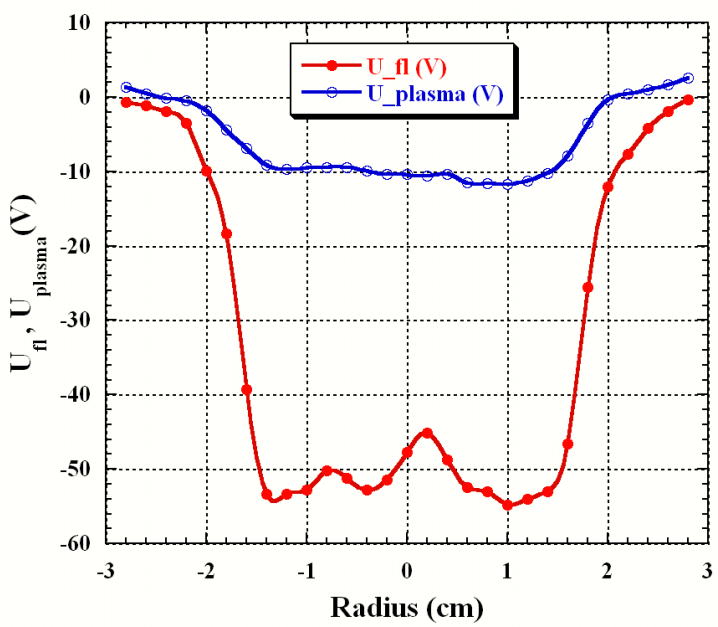

Figure 2.4: Typical Floating Potential and Plasma Potential Profiles in CLM ETG studies

The experimental region is about 150cm long, and typically has a background pressure of $\sim 10^{-6}\, Torr$ and $\sim 1 kG$ magnetic field, which leads to an effectively collisionless plasma. Multiple cryo-pumps are used to keep down the background pressure, removing both excess neutral particles fed in from the source region and neutral particles that result from the recombination of electrons and ions. A recent modification to the experimental cell is a moveable magnetic mirror coil. By varying the magnetic field produced by this coil, we can create a magnetic mirror trap in the front part of the experimental region, this area is referred to as the "mirror cell" or occasionally the "experimental cell". A more detailed explanation will be provided later on, but particles trapped in the mirror cell will undergo a net bounce-averaged curvature, and provide the basis for mixed slab-toroidal modes.

Numerous ports are located along the top and sides of the experimental region which allow for the insertion of various probes and diagnostics. At the end of the experimental region is an aluminum plate with a variable voltage bias. There is no confinement strong confinement in the axial direction, and a majority of the plasma will either recombine or be removed near the end plate. Depending on the instability being studied, the voltage bias on the end plate can be used to either trap different species by reflecting them back into the experimental region, or it can be used to subtly impact the plasma potential. Typical plasma parameters in the experimental region are listed in Table 2.1 below.

Magnetic Field	$B \approx 1kG$
Plasma Density	$n \approx 5x10^{8} - 5x10^{9}\ cm^{-1}$
Electron Temperature	$T_e \approx 20 - 25eV$
Ion Temperature	$T_i \approx 3 - 5\ eV$
Neutral Pressure in Cell	$P_n \approx 10^{-6}\ Torr$

Table 2.1: Typical Parameters in CLM

2.2 Generating Magnetic Curvature in CLM

In order to generate curved magnetic field lines in CLM, we make use of a moveable mirror coil located in the cell region. This mirror coil has existed inside of CLM for some time, and was used during similar mixed slab-toroidal ion temperature gradient (ITG) studies in the 1990's [41], but it had been unused since then.

The power supply and the cooling system had been misplaced, but we found a suitable 10kW current supply and created an air based cooling system. Precise records of the make and model of the mirror coil had been lost, but we were able to model the magnetic fields through a combination of experimental measurements and the physical size of the coil housing.

The mirror coil can be modeled as solenoid with a short finite length and thickness. Formal calculations aside, we measured the field along the axis experimentally using a hall-effect sensor mounted inside of a small enclosure that could be fit inside of the mirror coil

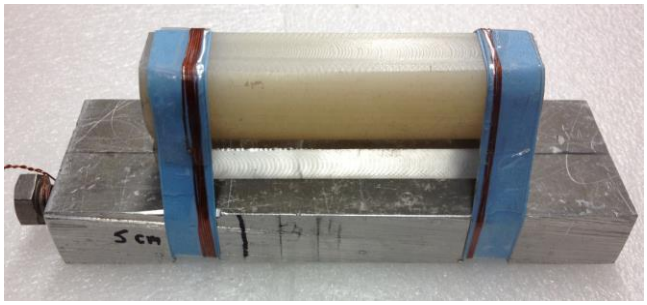

Figure 2.5: Enclosure Used for Inserting Hall Effect Sensor into the Mirror Coil.

We took a number of measurements at different mirror coil currents to ensure that the magnetic field scaled linearly, and we took the axial profile of the magnetic field at approximately ~1cm intervals. The experimentally measured field along the axis was able to be fitted approximately by using a simple Gaussian of the form:

$$f(x) = \frac{I}{150} * \frac{A}{\sigma\sqrt{2\pi}} e^{-\frac{(x-\mu)^2}{2\sigma^2}} \quad where\ A = 12, \sigma = 7.2, \mu = 7, I = current\ in\ coil$$

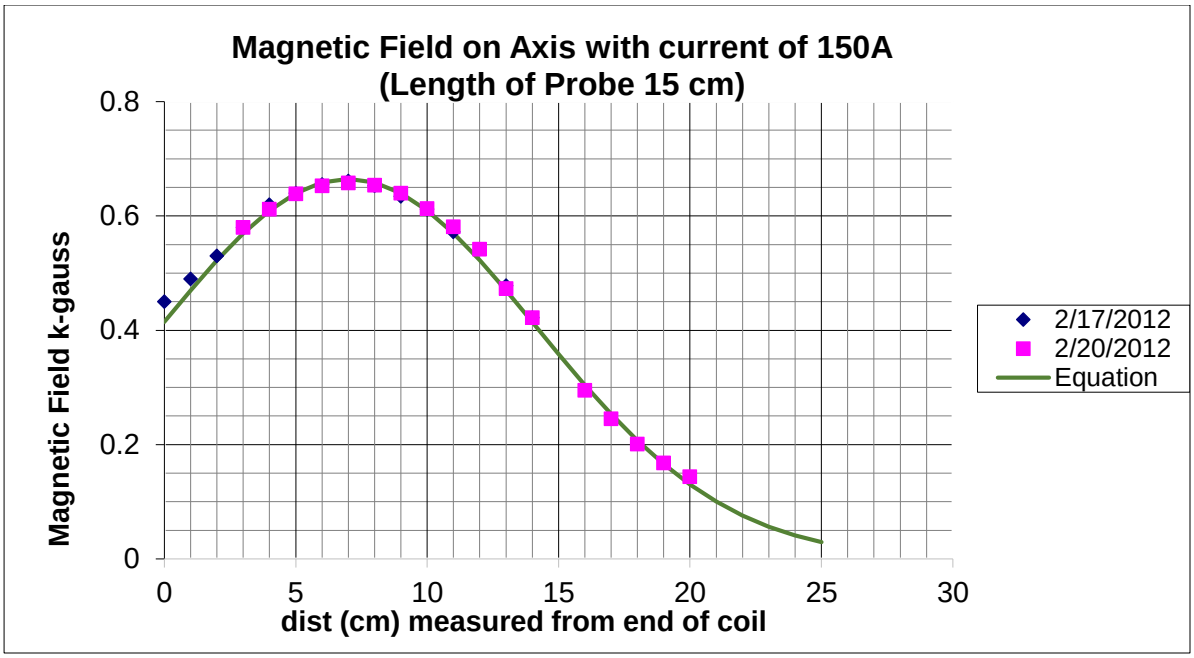

Figure 2.6: Magnetic Field due to Mirror Coil vs. Gaussian Appoximation.

It is worth noting that the Gaussian fit gives approximately the correct height and thickness for the magnetic field profile, but it will roll off too quickly on the tails compared to the magnetic field of an actual solenoid. The accuracy of the fitting was due to luck more than any inherent physics. Fortunately it is the general profile and not the tails that determine the dominant behavior of the mode. Later simulations using proper magnetic field modeling software found that a short solenoid with and inner diameter ~7cm, outer diameter ~11cm, and a length of ~14 cm (the same dimensions as the housing) and approximately $n = 50$ turns provided a similarly good fit along the axis.

Software was used to model the existing background coils in CLM as well as the effect of this new mirror cell coil as a series of solenoids. The profile due to the background magentic field coils already existed and had been used for prior studies, but while the machine was open a number of experimental measurements using similar hall effect proves verified the accuracy. A number of

different configurations involving different coil currents in the source vs. experimental region coils were considered, but the one chosen for the experiment was based on a large maximum mirror ratio and a relatively flat profile of magnetic field along experimental region.

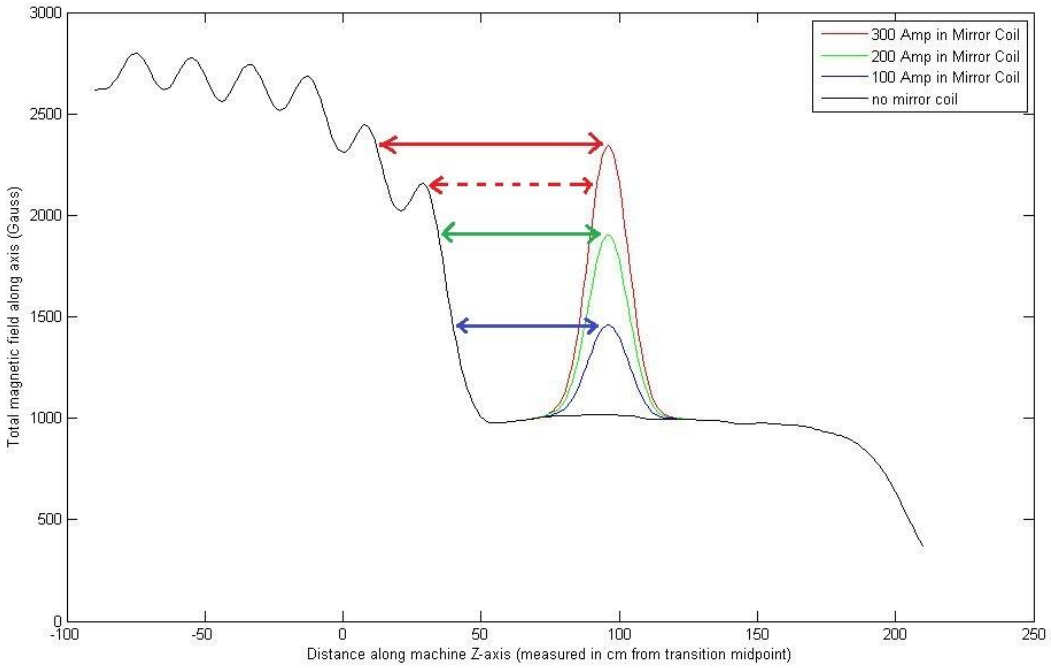

Figure 2.7: Magnetic Field for different mirror coil currents in CLM.

For a curvature driven mode, a parameter of interest in the radius of curvature. Our experiment emulates a well-known magnetic mirror trap configuration, and we can estimate the bounce averaged curvature as :

$$R_c = \frac{L_{cell}^2}{32 r_o (1 - R_m^{-.5})} \tag{19}$$

Where L_{cell} is the cell length (depicted by the arrows in Fig. 2.7), r_o is the radius of the mode off of the Z-axis, and R_m is the mirror ratio, defined as the ratio of the "peak" magnetic field divided by the "background" magnetic field in the experimental cell. [41].

As the current in the mirror coil increases, we simultaneously increase the mirror ratio and the mirror cell length. This effect comes from the slope of magnetic field along the transition region. The fact that L_{cell} increases with mirror ratio puts a practical limit on how much curvature can be obtained. This is outside of any "engineering" considerations and limitations of our power-supply and cooling methods. In practice there is an additional limit on the mirror ratio, $R_m < 2.2$ due to the mirror coil configuration of the cell region, beyond this limit the equation above breaks down entirely and you no longer have a single 'mirror cell'. For our experiment we operate well away from these limits, close to $R_{m,max}$~1.8, this is done because of limitations on CLM hardware, and to minimize the number of trapped particles.

Using the above information, we are able to compute the mirror cell length, mirror ratio, and approximate bounce averaged curvature as a function of mirror coil location, mirror coil current and background magnetic field in CLM. A typical set of calculations for different mirror coil positions used in our experiment is shown in Fig. 2.8 below:

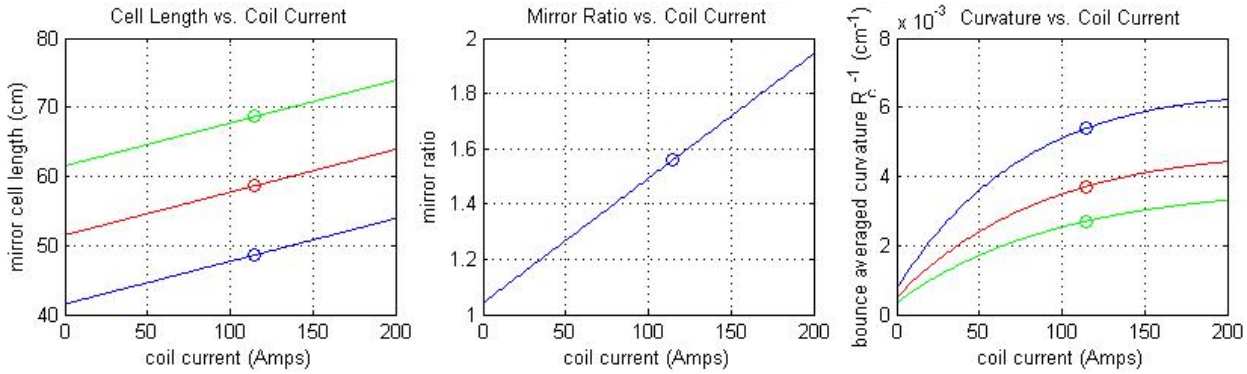

Figure 2.8: Cell Length, Mirror Ratio and Curvature vs. Coil Current

The mirror coil is placed at the end of a large metal pole, and there is a limited range of coil positions possible. In Fig. 2.8 we show mirror cell length, mirror ratio and bounce averaged curvature for 3 different mirror coil positions. The line in blue corresponds to the shortest mirror cell length, and hence the largest level of curvature, possible in CLM. The maximum mirror coil current is limited by the cooling system used. As a matter of practicality, trying to achieve coil currents larger than ~120 Amps for extended periods of time is unsafe for the equipment. This point of maximum coil current used in the experiment is denoted by a small circle in the figures above. In Fig 2.8 the plot of inverse radius of curvature assumes that we operate at a plasma radius of r=2.0 cm. This is because the typical ETG mode produced in CLM is well localized at about ~2cm. Unless otherwise noted, any references to inverse radius of curvature or curvature drive assume r=2.0cm, and plots and data that span across multiple radii will be labeled using R_m and L_c instead.

The maximum mirror ratio safely achieved in the experiment is about R_m~1.6, which is relatively small for a mirror trap. It is important to note that only trapped particles experience bounce-averaged curvature, and for ETG studies in CLM a majority of particles are not trapped. The trapping condition for a magnetic mirror configuration is given by $\frac{|v_\parallel|}{|v_\perp|} < \left(\frac{B_{max}}{B_{min}} - 1\right)^{-1}$, where $v_\parallel$ and $v_\perp$ are the parallel and perpendicular particle velocity components aligned either with or across the magnetic field lines and $\frac{B_{max}}{B_{min}} = R_m$ is the mirror ratio [32]. When electrons are represented as a distribution in velocity space, this is often referred to as the "loss cone", and particles with sufficiently high parallel velocity will be untrapped. It is worth noting that in a real plasma non-ideal field lines and occasional collisions can cause particles to enter and exit the loss

cone, but typically we assume particles are trapped if the above trapping condition holds, and if the mirror bounce frequency is much less than the collision frequency $\omega_{bounce} \ll \omega_{collision}$, together these ensure that individual particles will be trapped in the mirror cell and spend a significant time in the cell experiencing curvature before they are knocked into the loss cone.

Trapped particle fractions can be measured experimentally by using Langmuir probes to find plasma density inside and outside of the mirror cell. We can define a trapped fraction of particles as

$$Trapped\ Fraction = 1 - n_{outside}/n_{inside} \tag{20}$$

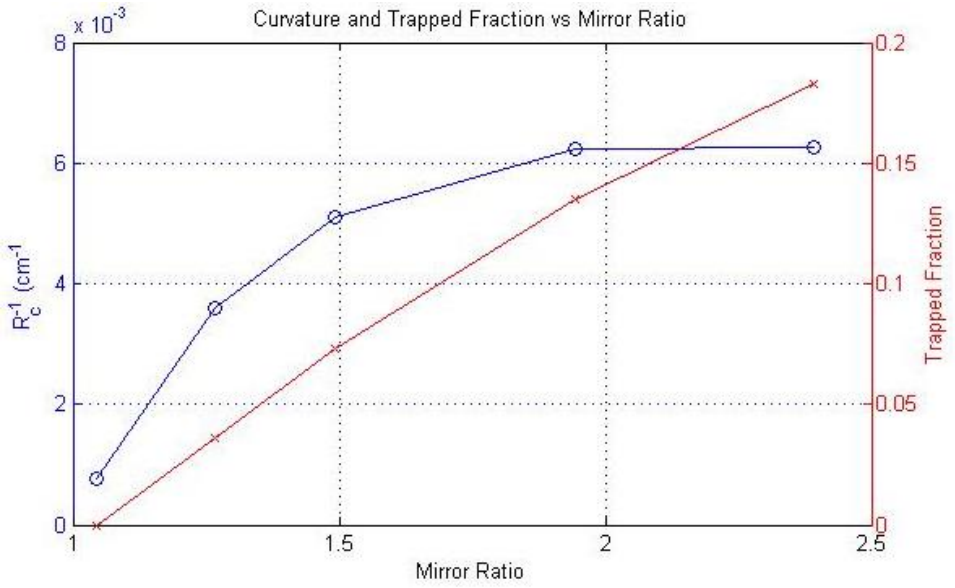

Figure 2.9: Trapped Fraction as a Function of Mirror Ratio and Coil Current

Figure 2.9 shows the trapped fraction of particles as a function of coil current and mirror ratio we find that it scales approximately linearly. For the mirror ratios used in ETG studies in CLM $R_{m.max}$~1.6, the maximum fraction of trapped particles is about ~8%, significantly smaller than the fraction trapped in a tokamak.

2.3 Diagnostics and Measurements in CLM

2.3.1 Overview of Diagnostics and Measurements

Diagnostics in CLM are primarily done with electrostatic probes directly inserted into the plasma through the diagnostic ports that line the top and sides of the machine. CLM has a long history of innovative probe and diagnostic design, but the current research makes heavy use of three diagnostics in particular: normal low frequency Langmuir probes, modified high-frequency Langmuir probes suitable for measuring ETG behavior, twin probes used for studying wave-structure and $k_{\perp}$, and triple probes used for studying radial thermal conductivity and electron temperature fluctuations. We will use this section to present some of the general theory behind our probes and diagnosics, including special considerations for CLM as a whole. A more detailed descriptions of high-frequency twin probe and triple probes along with their amplifier circuits and biasing schemes can be found along with the descriptions of experimental set-up for chapters 3 and 4 respectively.

Signals from diagnostics are typically acquired using a series of pre-amplifiers and amplifiers before being fed into an ADC. Once inside a computer, the signals can either be processed in near real-time using a suite of tools developed in LABVIEW, or the raw data can be saved and later processed using MATLAB or similar numerical software. With the notable exception of bicoherence, most of our processing techniques are based on either basic DSP filtering and time windowed Fourier transform analysis. Again further detail will be provided where needed along with the experimental results, but we will provide a brief overview of the processing used,

some of the special considerations for CLM, and an introduction to bicoherence and bispectral analysis.

2.3.2 Langmuir Probes in CLM

It is assumed that the reader is at least loosely familiar with the design and operation of Langmuir probes, but if not a good introductory resource can be found in [45]. Ion saturation current I_{sat} is obtained by inserting a conducting Langmuir probe into the plasma, biasing the probe with a high negative voltage ($\sim -150V$ in CLM), and measuring the resulting current through a small sensing resistor ($\sim 1k\Omega$). Typically ion saturation current fluctuations can be used as a proxy for density fluctuations. The floating potential can also be easily measured by connecting a sufficiently large resistor ($\sim 5M\Omega$) to the probe, along with the floating potential fluctuations. Normally we can compute the plasma potential from the floating potential by using the relation [45]:

$$U_{fl}(V) - U_{plasma}(V) = \frac{T_e(eV)}{2}\left(\ln\left(\frac{2\pi m_e}{m_i}\right) - 1\right) \tag{21}$$

Unfortunately, the above relation doesn't allow us to compute fluctuations in plasma potential in CLM. CLM contains a significant portion of hot electrons, and $U_{fl} - U_{plasma} \approx -E_{hot,e}$. But $E_{hot,e}$ only depends on plasma generation in the source region, which is independent of perturbations and fluctuations in the experimental region. Since $\tilde{E}_{hot,e} = 0$, we can't use the simplified relation above to measure fluctuations in plasma potential. Instead we use a method described in [46], and for hydrogen plasma we have:

$$\exp\left(\frac{-e\left(\phi_{plasma} - \phi_{fl}\right)}{T_e}\right) + \alpha\left(1 - \frac{e\left(\phi_{plasma} - \phi_{fl}\right)}{E_{hot,e}}\right) = .035 \tag{22}$$

Where α is the ratio of saturation current due to energetic electrons and bulk electrons, which is about ~1 in CLM. From the above equation the first order fluctuations will be given by:

$$\frac{\left(\tilde{\phi}_{fl}-\tilde{\phi}_{plasma}\right)}{\tilde{T}_e}=-\frac{\left(\frac{e\left(\phi_{plasma}-\phi_{fl}\right)}{T_e^2}\exp\left(\frac{-e\left(\phi_{plasma}-\phi_{fl}\right)}{T_e}\right)\right)}{\frac{\alpha}{E_{hot,e}}+\exp\left(\frac{-e\left(\phi_{plasma}-\phi_{fl}\right)}{T_e}\right)} \tag{23}$$

In the absence of electron heating from the disk and ring mesh we have $T_e \approx 8eV$ and $E_{hot,e} \approx 45eV$. This means that

$$\tilde{\phi}_{fl}-\tilde{\phi}_{plasma} \approx -0.1\tilde{T}_e$$

For typical values of electron heating we have $T_e \approx 15eV$ and $E_{hot,e} \approx 45eV$ which gives

$$\tilde{\phi}_{fl}-\tilde{\phi}_{plasma} \approx -0.4\tilde{T}_e \tag{24}$$

This provides us with an approximate value of $\tilde{\phi}_{plasma}$ from $\tilde{\phi}_{fl}$ and $\tilde{T}_e$, or for typical values in CLM we have that $\tilde{T}_e < \tilde{\phi}_{fl}$ and a very rough approximation can be given by $\tilde{\phi}_{fl} \approx \tilde{\phi}_{plasma}$. As a result, a large portion of the data presented in this thesis will be floating potential fluctuation measurements. It is worth noting that fluctuations in temperature cannot be measured directly by Langmuir probes, but a separate triple probe design can be used. However, Langmuir probes can be used to measure the equilibrium value of T_e.

Measuring the equilibrium electron temperature T_e requires a proper biasing circuit and the full $I-V$ characteristic curve for the probe. Generally the probe bias voltage is controlled through a computer using a DAC, and a full DC sweep is performed with a $\sim 1Hz$ speed, and the current can be taken through a sensing resistor and fed into a separate ADC.

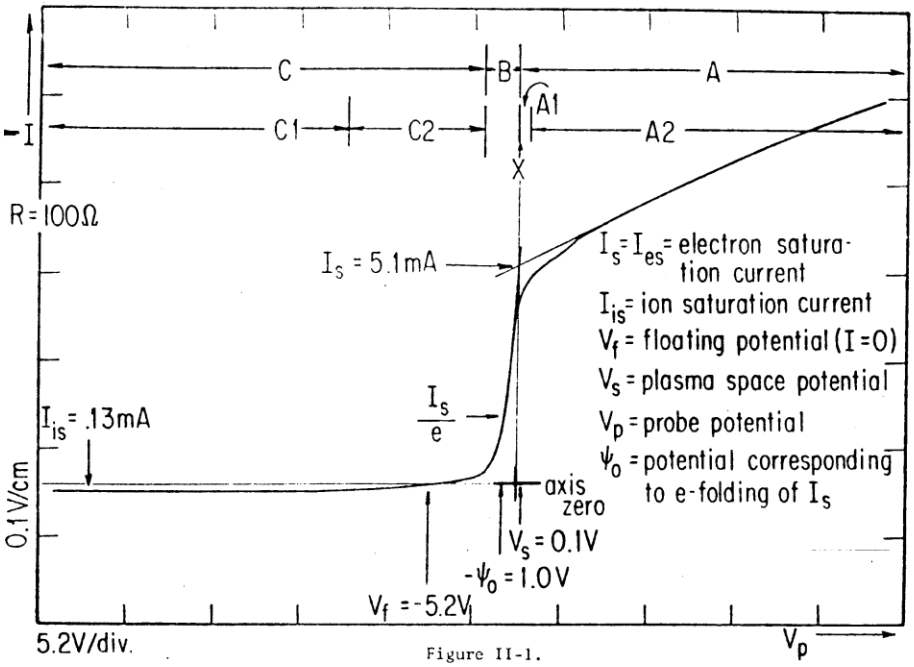

Figure 2.10: Typical I-V characteristic for Langmuir Probe

A full $I - V$ will provide information about ion saturation current for large negative bias voltage, and the e-folding part of the curve can be used to measure the electron temperature through the formula:

$$T_e(eV) = \frac{(V_2 - V_1)(V)}{\ln(I_2 - I_{sat}) - \ln(I_1 - I_{sat})} \tag{25}$$

Because there is a significant tail of hot electrons in CLM, we need to be careful with which part of the $I - V$ curve is used to make the fitting, and measuring bulk electron temperature will require the voltage range to skew slightly higher within the e-folding region.

Depending on the exact experiment being performed, more advanced probes and techniques can be used for acquiring signals related to potential, density and temperature fluctuations. But the methods are extended directly from traditional Langmuir probes, and in

practice Langmuir probe measurement have to be used to verify the equilibrium temperature and density profiles regardless of the specific experiment being performed.

2.3.3 Data Processing in CLM

A majority of the data processing in CLM falls under the category of either Short Time Fourier Transform (STFT) analysis, or bispectrum analysis. The STFT is a natural extension of the Discrete Fourier Transform (DFT). The DFT can be computed as

$$X_\omega = \sum_{n=0}^{N-1} x_n e^{-j\omega n/N} \tag{26}$$

And from Parseval's theorem the total power in the signal is given by

$$P_\omega = \left| \frac{1}{N} \sum_{n=0}^{N-1} x_n e^{-\frac{j\omega n}{N}} \right|^2 = \frac{X_\omega X_\omega^*}{N^2} \tag{27}$$

The frequency range of the output is determined by the Nyquest criterion $f_{max} < \frac{\Delta t}{2}$ and the frequency resolution is determined by the total signal length $T = N\Delta t$ and $\Delta f = \frac{1}{T}$. The main drawback of the DFT is that there is no localization in time, and the frequency components are taken over the entire signal.

To address this, the STFT can provide some localization in time, and can be used to investigate the time evolution of the spectrum. Intuitively the STFT divides the signals into multiple smaller time segments, and a DFT is computed for each segment. Segments are typically evenly spaced and overlap, and each segment is passed through either a Hanning window or Gaussian window to help localize the frequencies.

$$STFT\{x[n]\}(m,\omega) = X_{m,\omega} = \sum_{n=0}^{N-1} x_n \omega_{n-m} e^{-j\omega n/N} \tag{28}$$

Each DFT can be computed quickly using a fast fourier transform, and the result can be stored in a matrix with each column representing a frequency component and each row representing a different point in time. The main limitation of the STFT is that it has a uniform time and frequency resolution, unlike more advanced techniques using multi-scale analysis and wavelet transforms. However, the simplicity of the calculation and the fact that there are no pressing needs for efficient post-processing in CLM data means that the STFT is well suited for studying frequency components of the signal. The other benefits of the STFT is that it is easy to regain the DFT by simply each frequency component over all the time windows, and the STFT lends itself very nicely to bicoherence and bispectral analysis.

Obtaining a spectrogram from the STFT can be computed by simply taking the magnitude of the frequency components. To obtain a power spectrum, the spectrogram must be properly normalized to obtain physical units again.

$$Spectrogram\{x[n]\}(m,\omega) = \left|X_{m,\omega}\right|^2 = X_{m,\omega}X^*_{m,\omega} \tag{29}$$

And by averaging over all windows we obtain a spectra that is nearly identical to the original DFT. It is noted that the spectrogram produced is in terms of arbitrary units, and needs to be carefully normalized to regain physical units. The exact normalization depends on the method being used to compute the frequency components, but for the built in FFT function in MATLAB it is possible to simply use the window length for each sub-sample, *N*. All the code used was tested against a number of test cases to verify that Parseval's theorem held and that physical units were preserved.

To explore non-linear interactions between different frequency components we make use of bispectral analysis and bicoherence [47]. The bispectrum is normally defined as

$$B(f_1, f_2) = \langle F_{f_1} F_{f_2} F^*_{f_1+f_2} \rangle \tag{30}$$

Where $\langle \cdots \rangle$ denotes averaging. For frequency components with random phases, the three components will be completely decorrolated and average out to 0 for a sufficiently large number of samples. If the frequency components have correlated phases, the different samples will add together constructively. The use of f_1, f_2, and $f_3 = f_1 + f_2$ is because we are typically interested in interactions that satisfy the three wave coupling conditions: $\omega_1 + \omega_2 = \omega_3$ and $\vec{k}_1 + \vec{k}_2 = \vec{k}_3$.

To obtain bicoherence, the bispectrum must be normalized by an appropriate constant. There are a few competing definitions and constants used in literature, but the one commonly used in plasma physics comes from [47] and is defined as:

$$b^2(f_1, f_2) = \frac{\langle F_n(f_1) F_n(f_2) F_n^*(f_1 + f_2) \rangle}{\langle |F_n(f_1) F_n(f_2)|^2 \rangle \langle |F_n^*(f_1 + f_2)|^2 \rangle} \tag{31}$$

Where $F_a(f)$ denotes frequency component "f" of Fourier transform for sample "a". The bicoherence is calculating by averaging over many samples. In the case of CLM we typically use the STFT to provide the required samples. Each row of the STFT corresponds to a different point in time, and summing over ~100+ time samples provides sufficient accuracy.

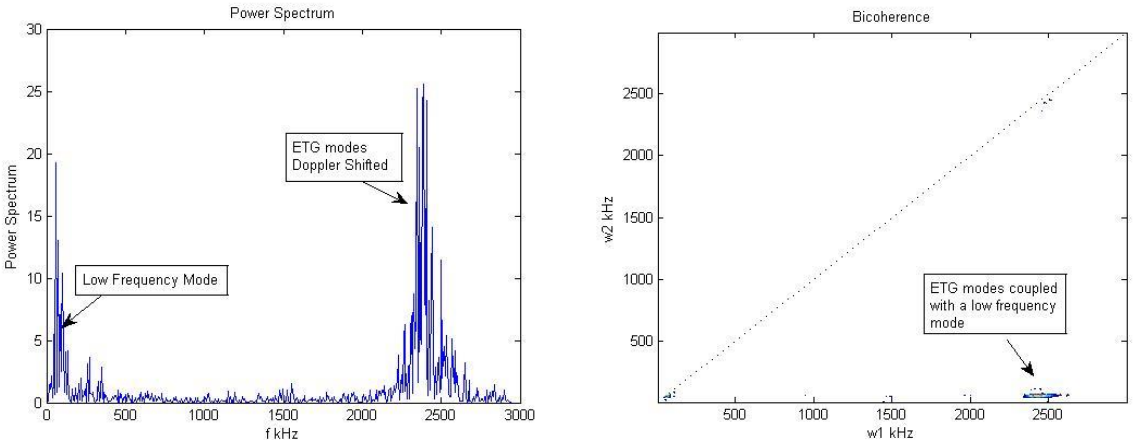

Figure 2.11: (a) A sample power spectrum and (b) corresponding bicoherence.

Prior work in CLM [38] have made good use of bicoherence to provide evidence of 3 wave coupling. For ETG studies typically we will use bicoherence to look for evidence of mode coupling between high frequency ETG modes and low frequency ion acoustic modes. The current belief is that low frequency ion acoustic modes act as a saturation mechanism and provide an energy sink via. Landau damping.

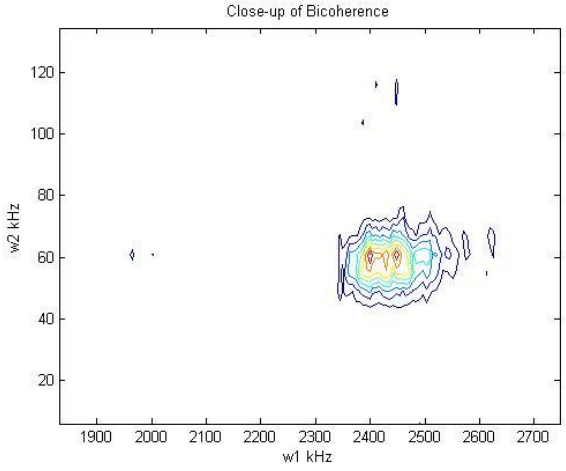

Figure 2.12: A close-up view of the plot from 2.11 part b showing bicoherence.

Zooming in on the section of the bicoherence that displays actual coupling we can exam the behavior carefully. It be seen that the high frequency modes are closely coupled to low frequency modes around ~60 *kHz* which is too low to be a result of $E \times B$ rotation but can be consistent with ion acoustic modes that exist in CLM and have $\omega \sim k c_s$. Under the present set of experiments we see similar coupling into low frequency modes, although the frequency of the low frequency modes occupies a wider range from ~50-150 *kHz.* Although we don't speculate too much on the nature of these modes, and instead direct the reader to the prior work by Tokluoglu et. al. these low frequency modes are consistent with ion dynamics whether they are all harmonics of Ion Acoustic modes in particular. We will qualitatively examine the level of coupling between ion and electron dynamics during the discussion on our mixed slab-toroidal mode scaling as one possible explanation of the significant increases in saturated ETG mode amplitude.

Chapter 3

Mixed Slab-Toroidal ETG Studies

3.1 Generating ETG

We refer the reader back to Chapter 2 for a general layout of CLM and a broad overview of the basing schemes. Generally we use a set-up similar to the slab ETG biasing found in [20], only with the added flexibility of a moveable mirror coil similar to studies in [41]. For this experiment we use CLM to produces a steady-state, quiescent, and near-collisionless hydrogen plasma with $n{\sim}5x10^{8} - 5x10^{9}\, cm^{-3}$, $B \approx 3\, kG$, $T_e \approx 20 - 25\, eV$ and $T_i \approx 3 - 4\, eV$. Our experimental parameters are sensitive to the vacuum conditions in CLM which may fluctuate slightly from day to day. We aim for as much consistency as possible, but there may be small changes in mode frequency and amplitude between run-days.

3.2 Measuring Temperature Profiles

To measure the temperature profile dependence on curvature, we first set CLM to operate with the maximum curvature possible by placing the movable mirror coil at the furthest position inside of the device. This corresponds to the blue line in Fig 2.8. Under these conditions, CLM operated with a cell length between ~45 to 56 cm and a maximum mirror ratio of ~1.6.

To obtain T_e measurements we used traditional Langmuir probes. LABVIEW was used to sweep the biasing voltage of the probe and measure the resulting probe current. Once the full I-V

curve was obtained LABVIEW can be used to find the appropriate e-folding part of the curve and compute the value of T_e. Each data point takes ~15 seconds to obtain, but since CLM operates in steady state this doesn't pose a serious problem. There is a limit on the maximum curvature that can be used since the mirror coil may overheat if we try taking multiple data points with very high mirror coil current. The experimentally obtained profile of electron temperature with and without applied curvature is shown in Fig. 3.1

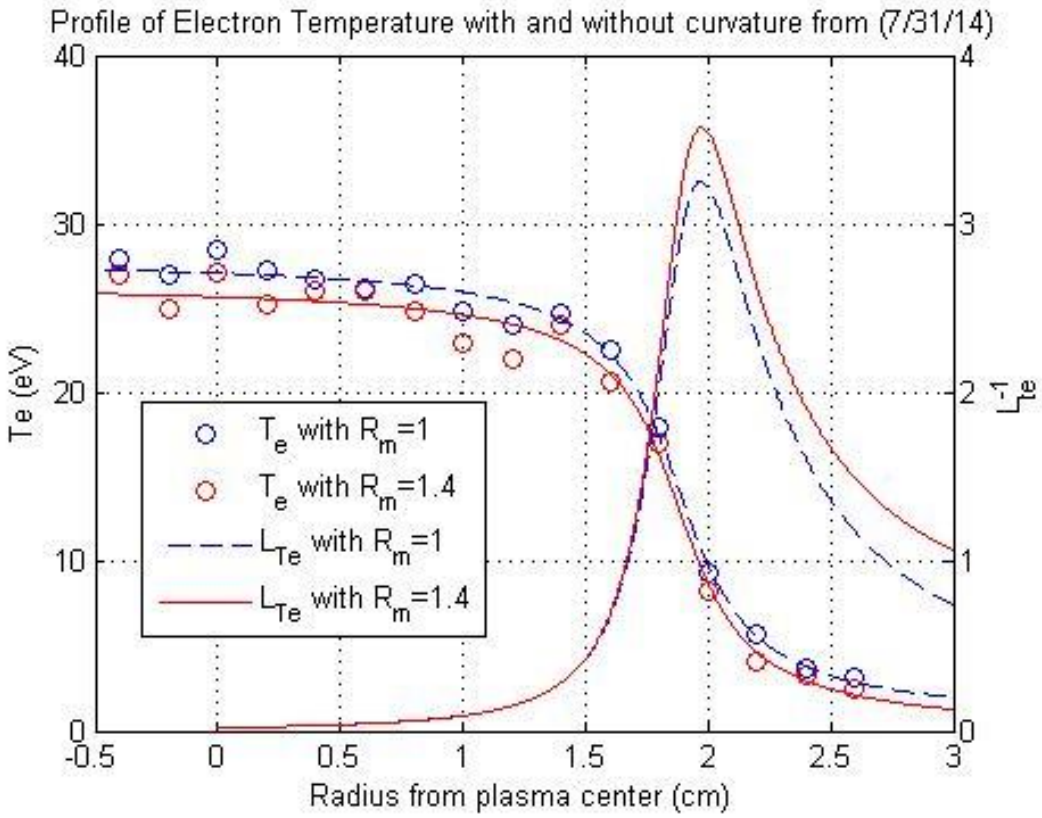

Figure 3.1: Profile of T_e Created Under Varying Mirror Ratio. The dotted blue curves are in the absence of curvature, and the red curves were taken with $L_c = 46cm$ and $R_m = 1.4$

The raw data points were obtained using a traditional Langmuir probe and calculated using LABVIEW. To calculate the gradient scale length $L_{Te}^{-1} \equiv \left|\frac{dT_e}{dx}\frac{1}{T_e}\right|$ we first fit the data using an

analytic function of the type $T_e \cong f(x) = a * \tan^{-1}(bx + c) + d$. The results of the fitting are shown in table 3.1, and the parameter values in parenthesis indicate 95% confidence intervals.

Fitting Parameter	No Curvature	$L_c = 46cm$ and $R_m = 1.4$
a	8.861 (8.062, 9.659)	8.574 (7.438, 9.71)
b	-4.614 (-5.979, -3.249)	-4.788 (-6.922, -2.653)
c	8.691 (6.191, 11.19)	9.005 (5.097, 12.91)
d	14.2 (13.41, 15)	13.17 (12.03, 14.31)
Adjusted R^2	0.9933	0.9852
RMSE	0.7612	1.1097

Table 3.1: Fitting Parameters for Temperature Profiles

From the fitting and the plots of Fig. 3.1 we find that the gradient drive L_{Te}^{-1} doesn't change substantially as we introduce curvature into the system. We require a sufficiently strong ETG drive $\eta_e = L_{Te}^{-1} > \eta_{e,crit} \sim 1$ in order to excite the mode [33], which is easily achieved in the region between r~1.8 and 2.3 with and without curvature. There is a very slight increase in the overall temperature and peak value of L_{Te}^{-1}, but this difference is only on the order of ~5-10%, and the effect of the increased curvature plays a stronger role in determining mode behavior. In both cases it can be seen that electron temperature begins to decrease around $r = 1.6\,cm$ but that the maximum of the gradient drive L_{Te}^{-1} occurs around r=2.0 cm. The data points shown for the curvature driven mode were taken with $L_c = 46cm$ and $R_m = 1.4$, which produces about 80% of the maximum curvature possible in CLM under the current experimental configuration.

3.3 Measuring ETG

Measuring ETG can be a challenge due to the high frequency and small spatial scales perpendicular to the magnetic field lines (large *m*-number and high $k_\perp$). ETG modes generated in CLM are typically ~Mhz in the lab frame, and our sensing diagnostics require sufficiently high frequency response and spatial resolution. To address this issue CLM has been equipped with specially designed probes. In figure 3.2 we show an example of the high frequency double-probe design used for ETG studies.

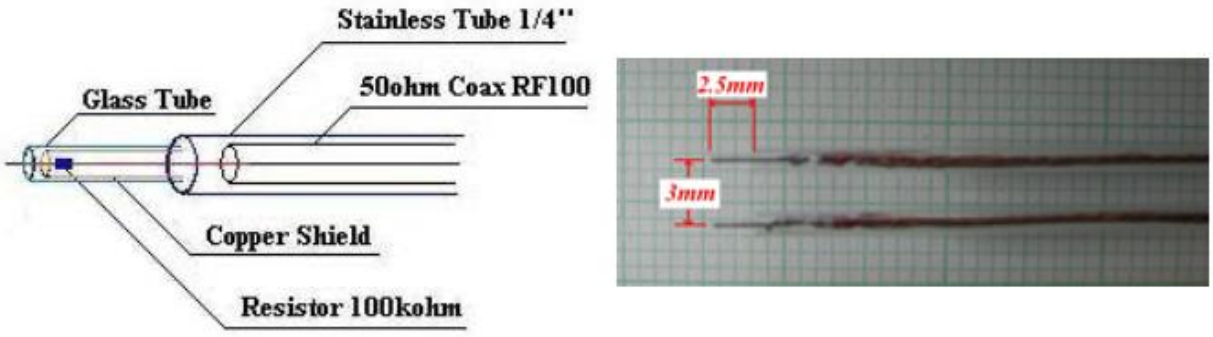

Figure 3.2: High Frequency Double Probe Design, and a Photo of the Probe

The probe has been designed with a surface mounted mini-resistor near the tip to minimize the input capacitance, and for a typical plasma sheath in CLM (~1pF) the probe has a frequency response of $1/2\pi RC \sim 10Mhz$. When inserted into the plasma column from the side, each of the double-probe tips will be at a slightly different azimuthal location separated by ~3mm, and by measuring the phase shift between the signals it is possible to identify azimuthal wave structure. Probes are typically biased to measure fluctuations in potential rather than density, and the

accompanying software and digitization hardware (LABVIEW system with NI-PCI-5122, 100MS/sec) has been chosen to have an equally fast response time.

Shots are obtained by first establishing a pure slab mode, and then slowly increasing the curvature by varying the mirror ratio. Since CLM operates as a steady state machine, shots can be of arbitrary length, but the typical record is ~1 second. For both slab and mixed slab-toroidal modes, a set of circular and annular meshes are used to accelerate the electrons, and the density in the transition region is large enough to thermalize the electrons and create a profile of electron temperature.

A typical output from the probe after processing is shown in Fig. 3.3. Signals are acquired for each probe tip separately, shown by the red and blue power spectrums. Typically the power spectra will be similar, although the relative size of the signals will be sensitive to probe orientation due to possible shadowing effects.

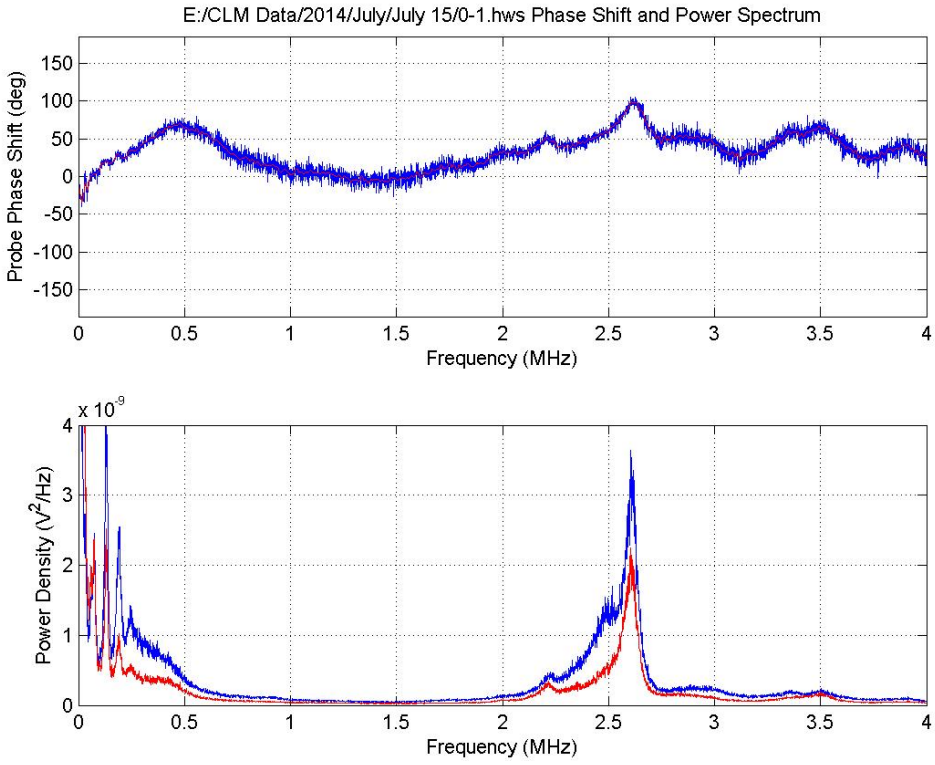

Figure 3.3: Typical Power Spectrum and Phase Shift Acquired by Double Probe.

The phase shift between the two probe tips is shown at the top of the frame. The phase shift between the two signals provides information about the azimuthal wave structure through the formulae:

$$m \sim \frac{\theta_{rad} r}{d_{tip}} \quad and \quad k_{\perp} = \frac{2\pi}{\lambda_{\perp}} = \frac{m}{r} = \frac{\theta_{rad}}{d_{tip}} \tag{32}$$

Where θ_{rad} is the phase shift between the signals in the probe tips, r is the radial position of the probe tips and d_{tip} is the distance between the tips. For the above figure we have $\theta_{rad} \sim \frac{100\pi}{180} = 1.75$, $r = 2.0cm$ and $d_{tip} \sim 3mm$ which gives $m = 11 - 12$ and $k_{\perp} \sim 5.5 - 6.0\ cm^{-1}$. These results are relatively typical, but depending on the exact plasma parameters ETG modes have been observed with $m = 10 - 14$ and $k_{\perp} \sim 5 - 7\ cm^{-1}$. this agrees with prior experimental work and numerical validations [20,21]

There is a small danger of aliasing when measuring the m-number using this method, since it is impossible for a single measurement to distinguish between θ_{rad} and $(\theta_{rad} + 2\pi n)\ n \in \mathbb{Z}$ this would occur for modes where $\lambda_{\perp} < d_{tip}$. It is possible to test for aliasing directly by rotating the twin-probe slightly. Since we have $k_{\perp} \gg k_{\parallel}$ the phase shift between the probe tips for a given orientation of the probe ϕ can be approximated as $\theta_{rad} = d_{tip}(k_{\perp}\cos(\phi) + k_{\parallel}\sin(\phi)) \approx d_{tip}k_{\perp}\cos(\phi)$ for $\phi \ll \tan^{-1}\left(\frac{k_{\perp}}{k_{\parallel}}\right) \sim 89^{\circ}$. By rotating the probe almost a full 90°, aliased modes would have their overall phase shift reduce to near-zero, and then significantly increase again as the effective tip-distance was reduced below the value of $\lambda_{\perp}$.

In practice we never see evidence of aliased modes in saturated steady state, and we only check occasionally for the sake of "due diligence". Simulations by the Horton group have found that modes in the range of $m{\sim}12-15$ will be dominant. And although it wouldn't be impossible to have an aliased mode with $m{\sim}30$, $k_{\perp}{\sim}15cm^{-1}$ and $\lambda_{\perp}{\sim}.4cm$, higher modes have spatial scales close to the machine Debye Length (~.15cm), and saturated coherent mode-structures should be many times larger than this scale length. Higher levels of aliasing with very large m-numbers are entirely unphysical for this reason.

A typical set of data will show ETG modes located between 2.0 MHz and 3.0 MHz in the lab frame, and a collection of low-frequency modes spanning between 0 and 500kHz. However, the ETG signals measured in the lab frame are Doppler shifted, due to the $\overline{\boldsymbol{E}} \times \overline{\boldsymbol{B}}$ rotation of the plasma column. To measure the frequency of the fluctuations in the plasma frame we can use the formula:

$$\omega_{lab} = \omega_{plasma} + m * \omega_{ExB} \tag{33}$$

It is worth noting that ω_{ExB} is sensitive to the radial electric field of the plasma, and it is sensitive to the plasma potential and plasma parameters. But typically we find $\omega_{ExB}{\sim}2\pi * 150\ kHz$. This value changes by about ~20% in either direction depending on plasma parameters, but normally it can be easily measured from the power-spectrum directly rather than trying to calculate it from Langmuir probe measurements of potential.

The peak around 2.6 MHz in the lab frame has been identified as a package of one or several ETG modes with varying azimuthal m-number, and the low frequency peaks have been previously identified as a combination of low frequency ExB mode ~150kHz, and sets of ion

acoustic (IA) modes that couple to the ETG modes and provide damping [38][48]. The initial study and verification of these modes was done previously.

3.4 ETG Scaling With Curvature

ETG mode scaling studies were loosely modeled after the work of [41,49]. To start we generate a curvature-free slab ETG modes based on methods developed in Ref. [20], and the curvature drive scaling, amplitude, frequency and radial structure was verified using Langmuir probe techniques.

After establishing the slab ETG mode, we would slowly ramp up current in the moveable magnetic mirror coil to establish different levels of magnetic curvature. For each level of curvature we acquire a full second of data to create our power spectrum.

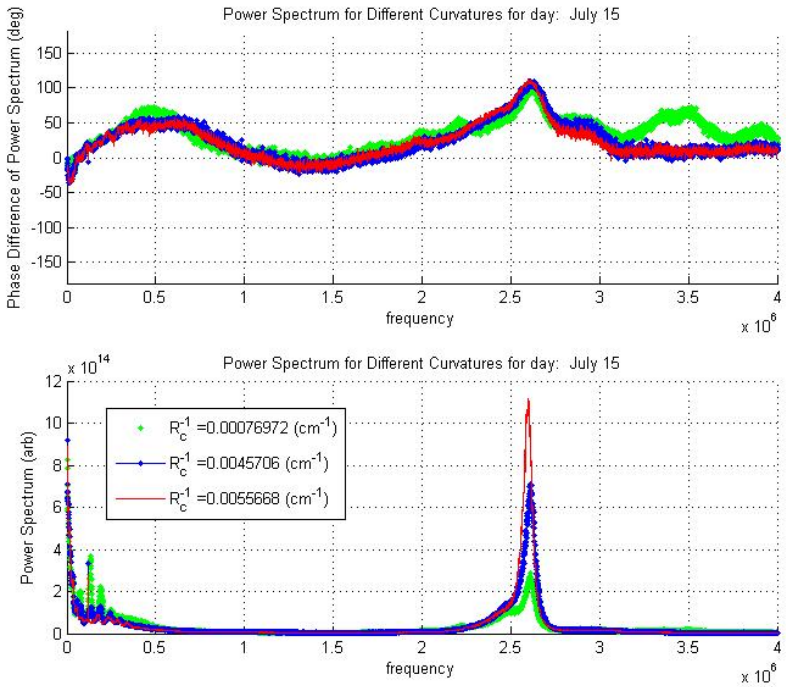

Figure 3.4: Power Spectrum (bottom) and probe phase shift (top) at a fixed radius r=2.0cm for different curvature levels.

A small subset of shots for different levels of mirror coil current and a fixed mirror coil location are shown in Fig. 3.4. This shows roughly the lowest level of curvature obtainable, the highest level of curvature obtainable, and an intermittent value of curvature with about ~75% of the maximum value is shown. It can be seen that in the lab frame the frequency of the mode is relatively stable, the saturated mode amplitude increases dramatically, and there are very slight changes in the measured phase-shift.

It should also be noted that there is a slight decrease in low frequency mode amplitude. One of the mode peaks corresponds to the $\boldsymbol{E} \times \boldsymbol{B}$ rotation of the plasma, and the other peaks are suspected to be ion-scale modes that provide non-linear damping for ETG via 3-wave coupling [18,25,38,48].

Around ~3.5 MHz we can see a very low amplitude mode form for the lowest levels of curvature. As the magnetic curvature is increased we observe a single mode peak becoming dominant, in this case the ~2.6 MHz mode. This effect may be a little easier to observe in the next where we present plots of the radial structure vs. curvature. The phase shift plot on the top of Fig 3.4 can only be interpreted easily for fluctuations with an amplitude significantly above the noise level, and phase measurements at 3.5 MHz are poorly defined for non-zero levels of curvature once the peak is attenuated.

3.4.1 Radial Structure of ETF with Curvature

Based on the similar temperature profiles with and without curvature from Sec. 3.2, it would be expected that the ETG modes would be strongest in within the radial range of r ~ 1.8 to 2.3 cm, where the gradient drive exceeds the critical threshold. To verify this we performed a series

of radial scans using our twin probes. The data was collected at 2mm intervals, with 3 sets of data (1 second each) for each radial location.

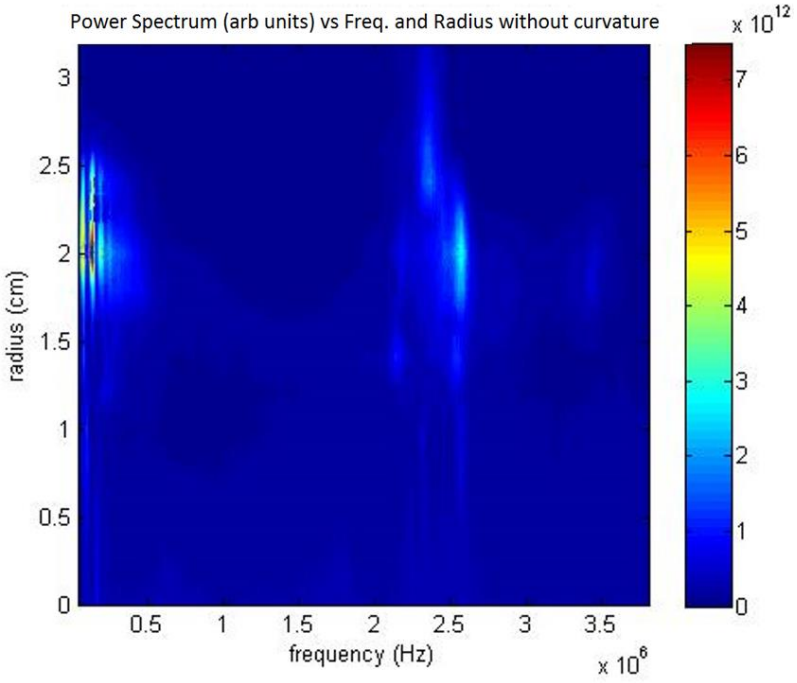

Figure 3.5: Power Spectrum at Different Radii Without Curvature.

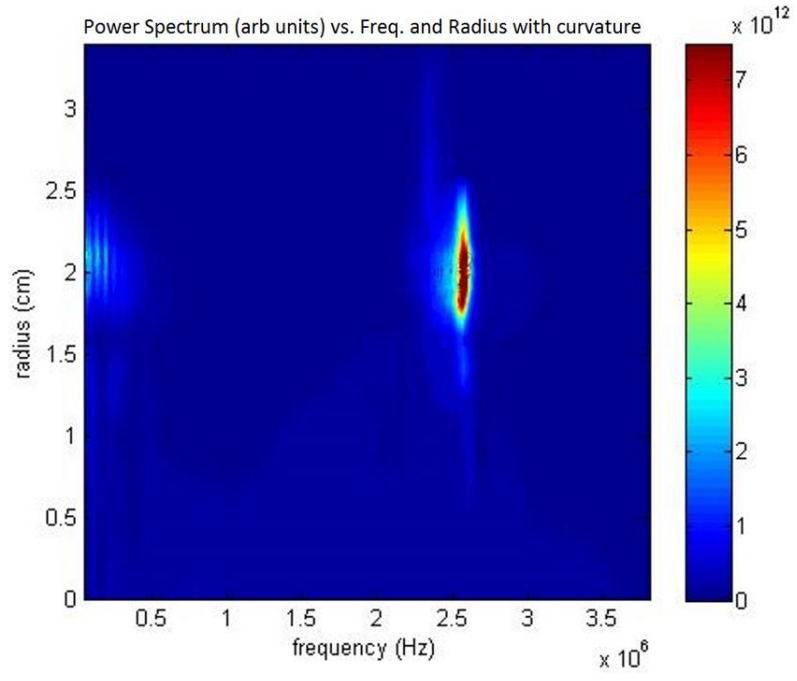

Figure 3.6: Power spectrum at different radii with a mirror ratio of $R_m = 1.46$ and $L_c = 47.3cm$ ($R_c^{-1} \sim 5x10^{-3} cm^{-1}$ at r=2cm).

Fig. 3.5 and 3.6 shows the radial and frequency dependence of the mode with and without applied curvatures. The horizontal axis is the frequency of the mode measured in the lab frame, and the vertical axis indicates the radial location. It can be seen that a ~2.6MHz ETG mode is radially located between r=1.8 and r=2.1, with a maximum peak close to r=2.0. This agrees with the estimates of L_{Te}^{-1} from the electron temperature measurements in Fig 3.1.

A series of low frequency modes <500kHz at the same radial location can also be seen. Prior work by Tokluoglu et. al. using bicoherence indicated coupling between low and high frequency modes as part of the ETG saturation mechanism [38]. With applied curvature we typically see a reduction in low frequency mode amplitude, and as we increase the curvature we see a single dominant ETG mode form, while other fluctuations at different frequencies and away from the peak in L_{Te}^{-1} appear to be suppressed. Still, the localization of the mode with and without curvature agrees well with the theory and temperature profile measurements.

3.4.2 Amplitude Scaling

In this section we will focus on the increase in power density and overall amplitude of the mode, and leave discussion of real frequency to the next section. Comparing results across run days requires some care. Depending on plasma parameters the exact frequency and amplitude of the mode may be quite different, even if the overall behavior is the same. Typically ETG modes are observed in the lab frame between ~2.1 and 2.6 MHz, alongside a series of lower amplitude low-frequency modes.

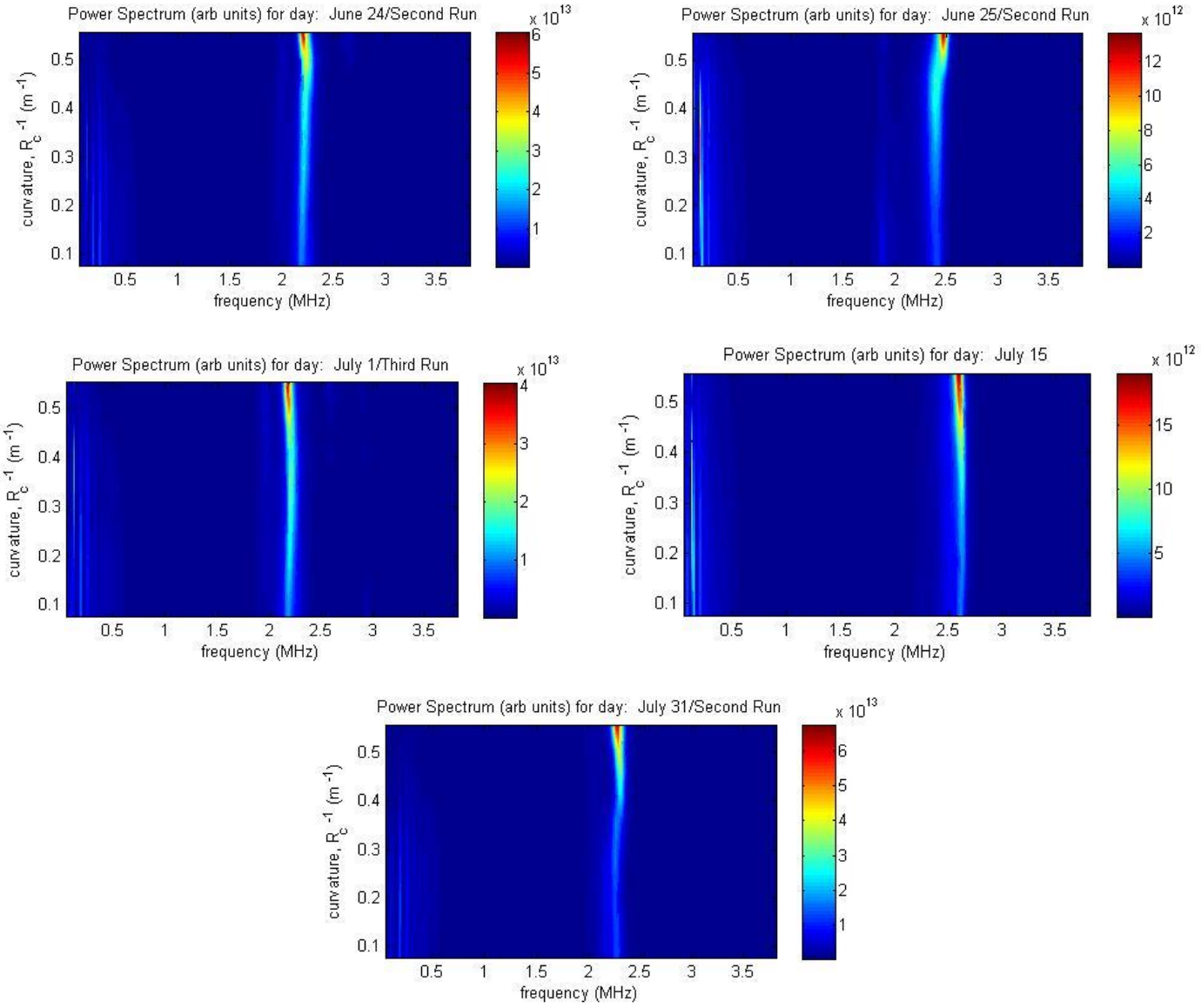

Figure 3.7: Spectrogram as a function of frequency (x-axis) and curvature (y-axis) for different run days and biasing.

Figure 3.7 shows a spectrogram of the mode under a number of different initial conditions and plasma parameters. It can be seen that there is a wide variance in the overall mode amplitude and lab-frame frequency, although the general behavior of slight wobbles in frequency coupled with a significant increase in amplitude as a function of curvature can be seen. Because there is a

large variance in frequency and amplitude, any quantified scaling will be slightly heuristic in nature.

For all of these run days we had identical background magnetic fields and mirror coil position (consistent with the discussion in section 2.2), anode bias ~60V, radial measurement location r~2cm and disk mesh bias ~20V. The exact plasma parameters will vary slightly from day to day with the quality of that day's vacuum conditions. By and large we operate in one of two regimes, one with lower mode amplitude that appears at ~2.3-2.4 MHz, and one with higher mode amplitude that occurs closer to ~2.5-2.6 MHz. Each of these regimes have slightly different $\boldsymbol{E} \times \boldsymbol{B}$ frequencies associated with them, but it is found that they both behavior very similarly in terms of overall scaling and general behavior.

There are a few ways to characterize the amplitude of the mode, but we will start by tracking the peak power density mode for different curvature levels. This was done by running a quick smoothing filter across the data to suppress noise, and then finding the maximum value of the mode peak for different levels of curvature. The results are displayed below:

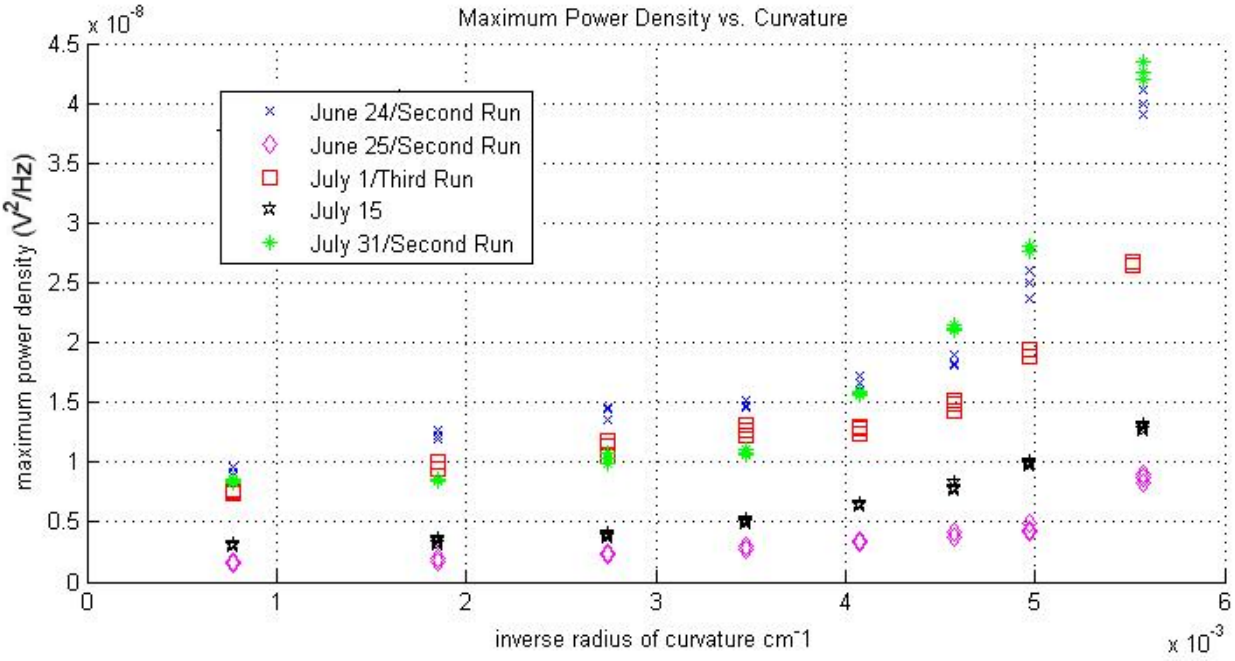

Figure 3.8) Maximum Mode Power Density vs. Curvature

In Fig. 3.8 we show the scaling of the peak power density of the mode as a function of curvature over a wide range of run-days and initial conditions. Generally the peak power density shows only a modest increase for small values of curvature, and then displays significant growth above $R_c^{-1} \sim 4.5x10^{-3} cm$. All of the above experimental runs were taken with the same minimum mirror cell length possible in CLM, represented by the blue curve on Fig. 2.8 and slightly different levels of background plasma density and potential.

From our basic fluid theory we would predict slight increases in mode growth rate γ as a function of curvature, on the order of 10% or so. Simulation results for ETG by Jenko and Dorland [7,10] find that saturated mode for ETG scale as $\propto \gamma / k_\perp^4$ for the fastest growing modes. Based on our experimental measurements we would expect only small changes in overall mode amplitude.

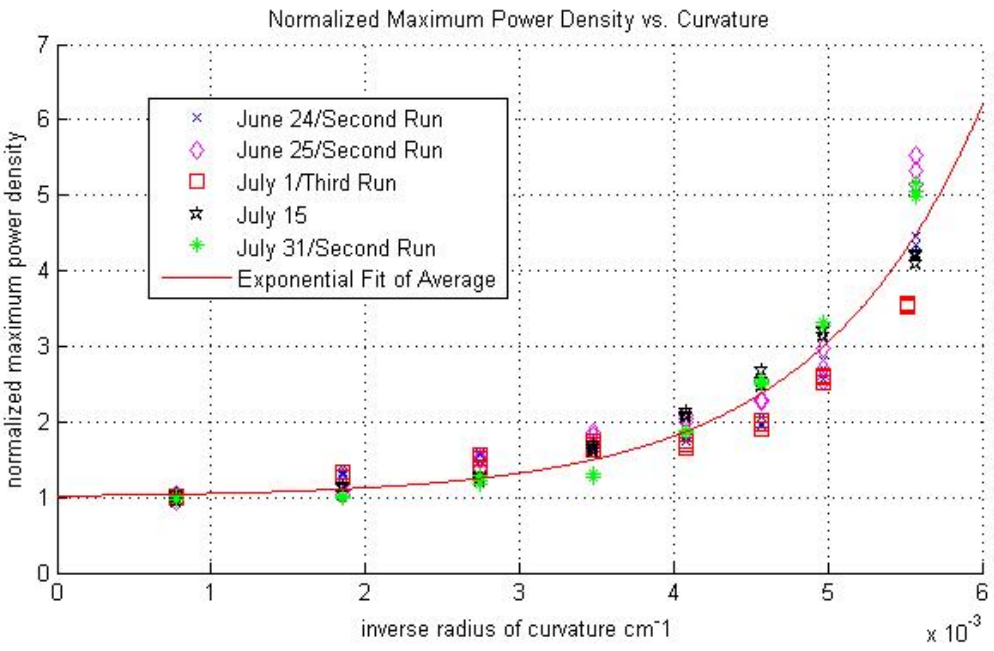

Figure 3.9) Maximum Mode Power Density vs. Curvature Normalized

Fig. 3.9 shows to same data, but normalized to compare growth rates across different run days. For each run, we divide all the data by a single coefficient such that the average value of the minimum curvature data point has a power density of 1. It can be seen that the data generally follows the same exponential growth rate regardless of the initial conditions chosen. Fitting an exponential of the type $f(x) = ae^{bx} + 1$ for all the data yielded coefficients of a=0.197 and b=928.6, sse=10.19 and an effective rsquare = .93163. This indicates a relatively good fit for the data, and provided a lower error level than quadratic or cubic regressions (sse 18.12 and 10.56 respectively).

To find the total amplitude of the fluctuations we first integrate the power spectrum across the region of interest, and then take the square root to find the equivalent RMS voltage level.

$$\tilde{\phi}_{rms} = \sqrt{\int P(f)\, df} \tag{34}$$

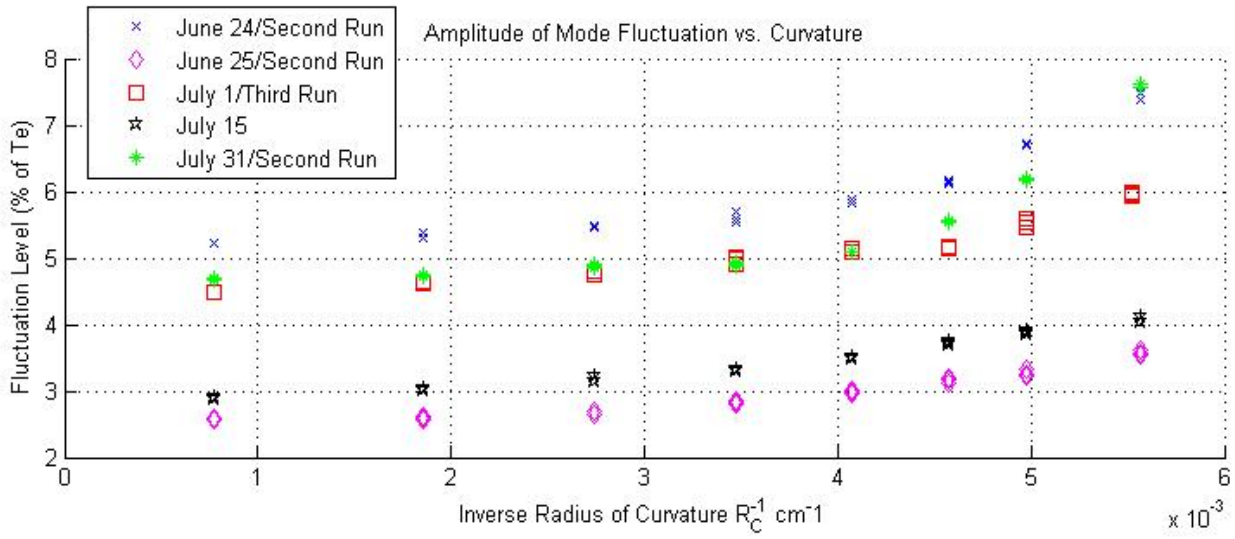

Figure 3.10: Fluctuation levels as a percentage of electron temperature $\tilde{\phi}/T_e$

In figure 3.10 we present the total amplitude of the fluctuations as a percentage of electron temperature. This was done by first computing $\tilde{\phi}_{rms}$ by integrating the power spectrum from ~2Mhz - 3Mhz to obtain the full power in the ETG modes. The result needs to be multiplied by a fixed constant to account for attenuation between the probe and the digitizer, as well as the factor of $\sqrt{2}$ between amplitude and root-mean-squared. In practice the method was checked by running the MATLAB code against a few known test cases fed directly from an oscilloscope into the probe. The value of T_e for the above calculation was assumed to be a fixed 20V.

For the overall fluctuation levels we see a more modest increase in amplitude of potential fluctuations on the order of $\frac{\tilde{\phi}_{curvature}}{\tilde{\phi}_{slab}}$ ~1.5, which would still exceed $\propto \gamma/k_{\perp}^4$ a scaling suggested by [38]. This would suggest that our saturated ETG modes amplitudes are increasing, which is

consistent with higher growth rates predicted by fluid and kinetic theory, the combination of linear growth rate theory and $\propto \gamma/k_{\perp}^{4}$ amplitude scaling from simulation is unable to account for the size of this change.

3.4.3 Azimuthal Structure and Frequency Scaling

The frequency of the mode is stable in the lab frame across this range of curvature, typically deviating only $\pm 20kHz$ in the lab frame and maintaining similar $k_{\perp}$ and m-number. Careful measurements of the phase shift between the two signals shows a slight increase for larger values of curvature. This indicates a move to slightly higher *m*-number. A careful examination of the low frequency component also shows a slight reduction in the $\overline{\boldsymbol{E}} \times \overline{\boldsymbol{B}}$ rotation, measurements of the potential profile are relatively stable across different frequency ranges, but this could be explained by the increase in overall magnetic field will reducing the average electric field drift velocity $v_E = \frac{\boldsymbol{E}\times\boldsymbol{B}}{B^2}$.

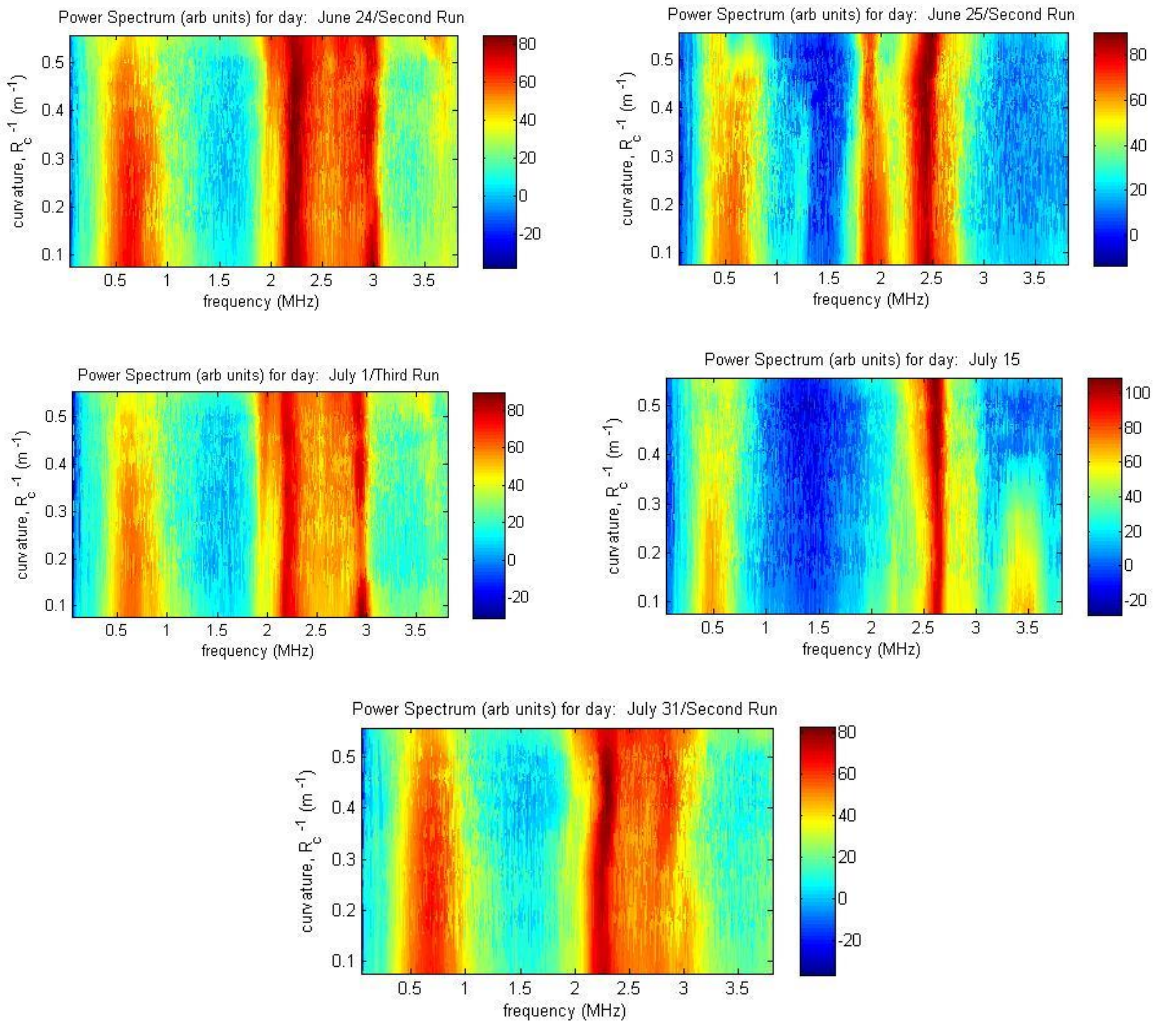

Figure 3.11: Phase between probe tips as a function of frequency (x-axis) and curvature (y-axis) for different run days and biasing.

A careful examination of the phase shift between the probe signals indicates that there are very small changes in the phase shift along with increased frequency, on the order of about ~10% if we follow the path of the strongest coherent mode structure.

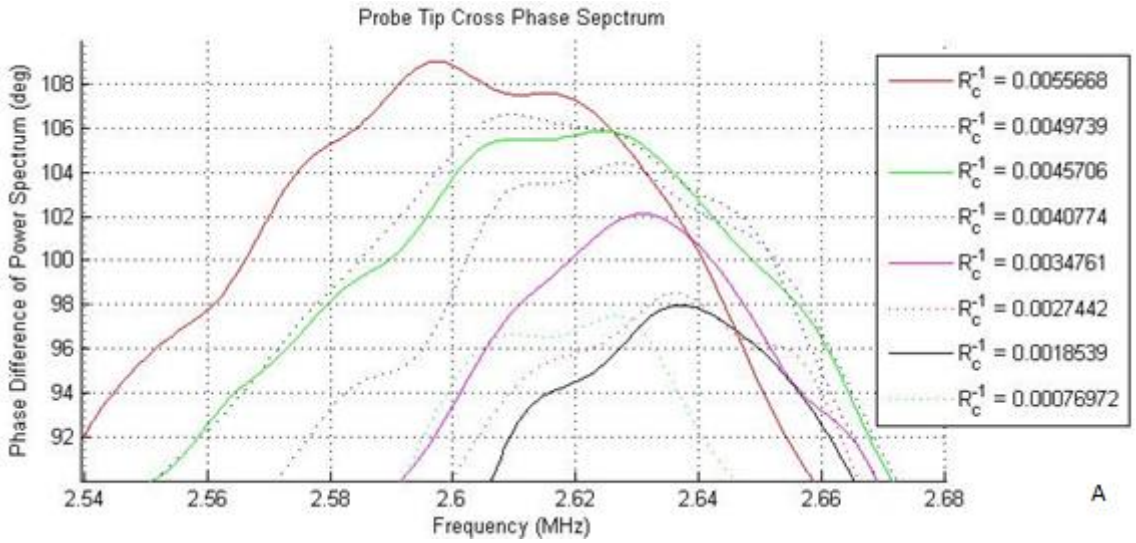

Figure 3.12 (A): Phase Shift as a Function of Curvature for a Specific Run Day

Examining a single run-day carefully, we can see that there is a small but significant increase in the phase shift between the probe tips. In Fig. 3.12A we see that the phase shift increases from ~96 degrees for pure slab modes to ~107 degrees for the highest levels of curvature. From the discussion in Sec. 3.2 this would suggest an increase in the *m*-number of the mode from $m_{slab}\sim 11.17$ to $m_{curvature}\sim 12.45$. This is a small change, but there is nothing in the linear theory that would inherently suggest an increase in *m* number.

The validation work done by Fu. simulating the slab ETG mode in CLM [21] showed that a dominant $m\sim 12$ structure would appear in steady state, as shown in Fig. 1.2. The physics behind this was highly non-linear, and was a result of the combined plasma parameters and boundary conditions in CLM. The GTC code [22] used was adapted from tokamaks, and simulations need to specify a major radius *R* in order to run, which is analogous to R_c in our slab geometry. Most of their "slab" simulations were run with $R\sim 3m$, the approximate length of the full CLM vacuum chamber. As an aside within [21], they ran a simulation with $R\sim 1m$, effectively changing the value

of R_c from $R_c^{-1}{\sim}3x10^{-3}cm\ to\ R_c^{-1}{\sim}10x10^{-3}cm^{-1}$ and found that the m-number was increased from 12 to 15. Although it is difficult to make a direct comparison, our observed increase in *m*-number with curvature and the general values roughly agree with the prior simulations.

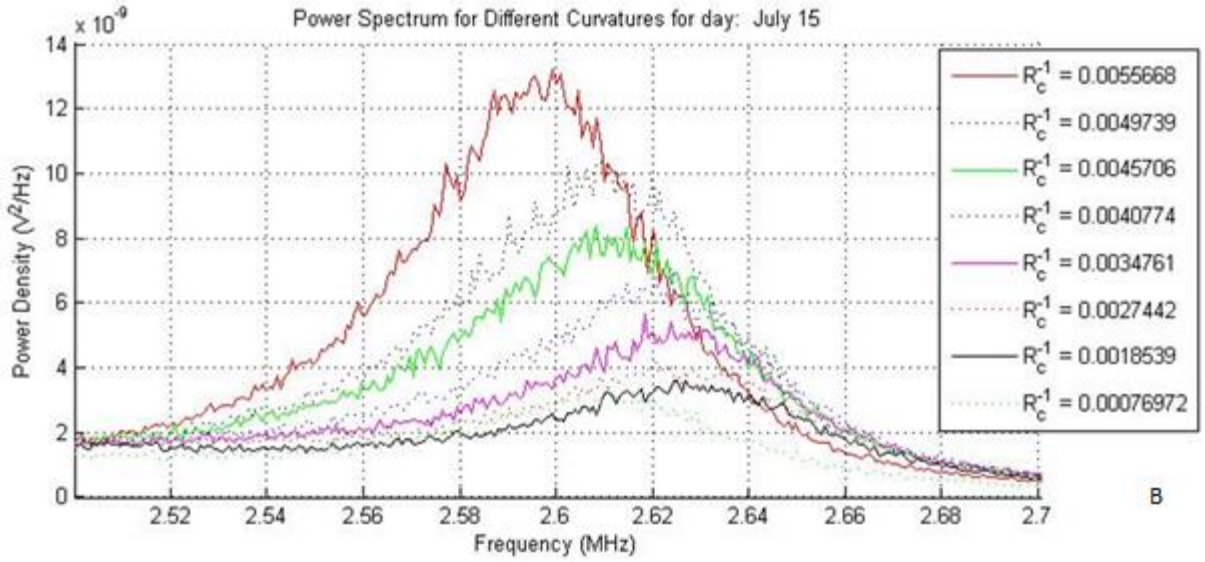

Figure 3.12 (B): Mode Peak as a Function of Curvature for a Given Day

An increase in m-number also implies an overall increase in the Doppler shift for the mode observed in the lab frame, but most of our data shows a slight decrease in real frequency. A rough calculation of the plasma frame frequency as a combined function of m-number and lab frame frequency shows a slight decrease with curvature.

R_c^{-1}	ω_{ExB}	Lab Frame Freq.	Phase Shift	m-number	Plasma Frame Freq.
0.7697	150	2610	96.5	11.22828485	925.7572718
1.8539	150	2627	98	11.40281778	916.577333

2.7442	150	2623	98.5	11.46099542	903.8506868
3.4761	150	2625	102	11.86823891	844.764163
4.0774	150	2620	104	12.10094948	804.8575779
4.5606	150	2612	105.5	12.27548241	770.6776391
4.9739	150	2610	106.5	12.39183769	751.2243466
5.5668	150	2597	108	12.56637061	712.0444078

Table 3.2: Sample Calculation for Changes in mode Freq.

The measurements are a little rough, and comparisons with theory are also complicated since the precise value of ω_{de} will change with the changing m-number as well. But most of our data indicates slight changes in the overall plasma frame frequency on the order of ~20%. From our fluid theory and from kinetic theory [33] increases in curvature will lead to the fastest growing modes having smaller values of $k_{\|}$. This reduction in $k_{\|}$ corresponds to a similar down-shift in real frequency. This can be seen from the fluid model plots, or it can be seen in kinetic dispersion relations since the resonance condition $\omega \sim k_{\|} v_{te}$ dominates for modest levels of curvature.

3.4.4 Changes in Parallel Wave Structure

A simple experiment has been designed to measure changes in in the parallel wave structure. Two high frequency Langmuir probes similar to the design used in Fig 3.2 are placed approximately 7cm apart through a port along the side of CLM. The tip of the probe is placed slightly off-center, and rotating each probe can be used to fine-tune the azimuthal probe location.

The distance between the probes is approximately 7cm, although there is a slight variance of up to ~2mm based on the rotated position of the probes.

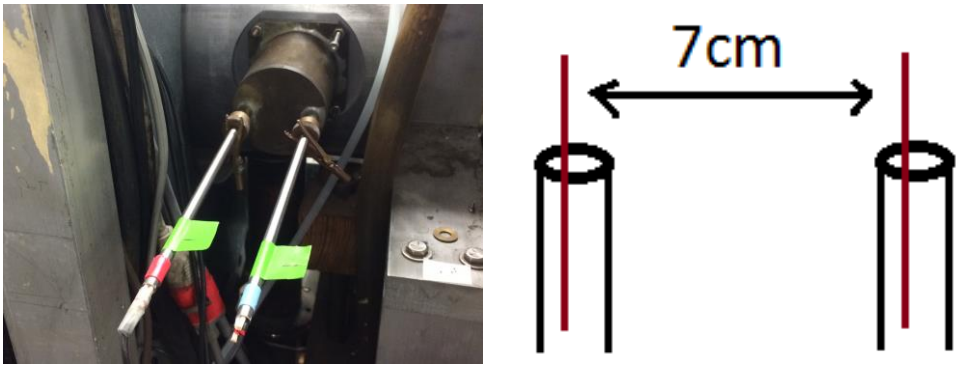

Figure 3.13: Probes used in CLM for measuring $k_{\parallel}$

The phase shift between the two probe signals can be modeled similar to the measurements for m-number using the formula $\theta_{rad} = d_{tip}(k_{\perp}\cos(\phi) + k_{\parallel}\sin(\phi))$, and for a perfect alignment we have

$$k_{\parallel} = \frac{2\pi}{\lambda_{\parallel}} = \frac{\theta_{rad}}{d_{probes}} \tag{35}$$

Because $k_{\perp} \gg k_{\parallel}$ for both slab and toroidal modes, a reliable absolute measurement for $k_{\parallel}$ requires a very high level of alignment accurate to within 2 degrees. It is slightly easier to measure changes in $k_{\parallel}$ since the inaccuracy added from the contribution of $k_{\perp}$ will largely cancel out if you subtract the phase measurements from one another.

Alignment was done by first creating a conducting plasma and then finding the location where the impedance between the probes was minimized, since the minimum impedance would be along a single magnetic field-line and hence be purely parallel to the field lines. This method provides a decent level of accuracy, but it is limited by the accuracy of our millimeters as well as

the fluctuations of the plasma. A second method for aligning the probes involves supplying a high level of curvature, and trying to minimize the overall phase shift between the two modes. Since toroidal modes are expected to be flute-like with $k_{\|}\sim 0$ a properly aligned set of probes should have zero phase shift from the perpendicular component and close to zero phase shift from the parallel component. This provided a good internal check on the alignment produced by impedance measurements.

A number of experimental limitations put a halt to the experiment before a full scaling could be obtained, and even under ideal circumstances the level of change in parallel wave-number is close to the limits of our accuracy. Still, early results indicated a slight reduction in $k_{\|}$ on the order of the change found in ω in the plasma frame.

3.5 Three-Wave Coupling with Curvature

Three wave coupling between two ETG modes and a third ion acoustic mode has been proposed previously as a non-linear damping mechanism, and this has recently been proposed as a general source of damping for drift wave turbulence [38,48]. By examining the bicoherence of the mode for varying levels of curvature we can try to identify any types of qualitative changes.

The bicoherence was run using data from our normal twin-probe measurements. We had a frequency resolution of ~3kHz and about 1500 frames. Each computation is intensive, but it can be run on a standard desktop computer on a reasonable ~5min time frame.

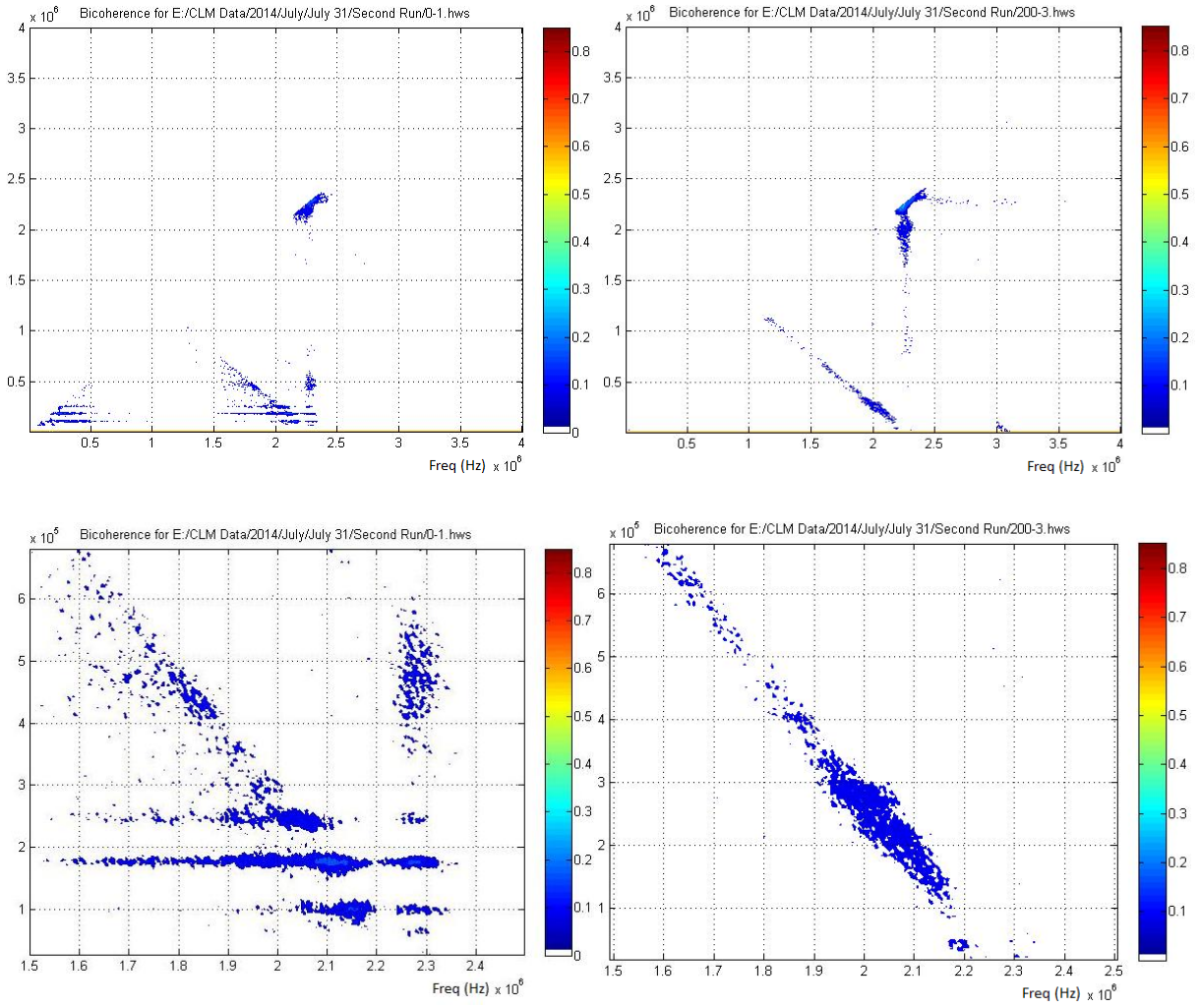

Figure 3.14: Bicoherence with and without curvature for a specific run-day. On the left, minimum curvature, on the right is maximum curvature. The bottom images are zoomed in views of the coupling between high and low frequencies.

In Fig. 3.14 We show a typical bicoherence output for a single set of data under maximum and minimum levels of curvature. Under slab conditions we find moderately strong coupling between low frequency modes and frequencies in the ~2.0 -2.3 MhZ range coupling into the main ETG peak. Although we didn't have the proper low-frequency diagnostics to determine the exact

nature of the low frequency modes, the lower frequencies suggest ion-scale dynamics, and the finding isn't inconsistent with prior results [38,48] showing coupling into ion acoustic modes.

For higher levels of curvature the coupling picture changes, and rather than having a few discrete low-frequency modes, we instead observe coupling into a wide "smear" of frequencies. We also note that there is also increased self-coupling between high frequency ETG modes into even higher frequency modes. Trying to comment exact nature of the coupling would be speculative at best. Within the existing theory arguments can be made that slab-modes are coupled into discrete ion-acoustic type modes, while mixed slab-toroidal modes begin to interact with longer wavelength interchange or Raleigh Taylor modes, but a full investigation is beyond the scope of this research. Still, at the very least our experimental measurements would suggest that the mechanism of mixed slab-toroidal modes might be a fruitful area of research for simulation and theory.

Chapter 4

Radial Transport due to Mixed Slab-Toroidal ETG

4.1 Theoretical Background on Radial Transport

Radial thermal flux due to ETG modes is a source of energy loss for magnetically confined plasmas. In classical/neo-classical theory diffusion across field lines is driven by collisions, and is predicted to scale as $\sim 1/B^2$. In practice, early experiments in the 1940's and 50's found that losses followed Bohm diffusion, $D_{Bohm} = \frac{1}{16}\frac{(k_B T)}{eB}$ which scales as $1/B$. In practice, Bohm diffusion sets the "worst case" upper limit for diffusion in magnetically confined plasmas, while Gyro-Bohm diffusion $D_{GB} = \frac{\rho}{L} D_{Bohm}$ where $\rho = \frac{m v_\perp}{|q|B}$ is the Larmor radius and L is the gradient scale length of interest, has the same $\sim 1/B^2$ scaling as classical diffusion and sets a theoretical lower bound. In practice the experiments operate between these two limits of Bohm and Gyro-Bohm with a scaling between $\sim 1/B$ and $\sim 1/B^2$.

The difference between the lower bound of classical diffusion and experimentally measured diffusion rates is deemed "anomalous transport", and it is typically attributed to micro-turbulence and drift waves. The actual transport mechanism comes from correlated fluctuations in density, temperature and velocity [50]:

$$Q_{r,i} = \langle nT\tilde{v}_r \rangle \approx \frac{3}{2} T \mathrm{Re}\{\langle \tilde{n}\tilde{v}_r \rangle\} + \frac{3}{2} n \mathrm{Re}\{\langle \tilde{T}\tilde{v}_r \rangle\} \cong Q_{conv} + Q_{cond} \tag{36}$$

Uncorrelated fluctuations in velocity and temperature/density would average out to 0. There would be peaks and valleys, but no net flux over time. But if fluctuations are correlated a net flux of thermal energy or particles can move out of your system. One key motivation for understanding how to predict, control and mitigate drift wave turbulence is to reduce these anomalous fluxes, and to achieve a better confinement closer to the Gyro-Bohm limit. For ETG [29,37] typically the convective flux is much smaller than the conductive flux, and the anomalous electron thermal flux due to these fluctuations is given by

$$\Gamma \cong \frac{3}{2} nRe\langle \tilde{T}\tilde{v_r} \rangle \tag{37}$$

As before, we use $\langle \cdots \rangle$ to denote cross-correlation of the variables when represented in complex notation. For drift waves we can assume that the plasma potential fluctuation has the form $\tilde{\phi}_p \sim f(r)e^{i(m\theta + k_\parallel z - \omega t)}$ where $f(r)$ is a function or radius, m is the azimuthal wavenumber and the other variables have standard interpretations. For fluctuations of this type we can rewrite velocity as a function of the plasma potential

$$\tilde{v_r} = \frac{c\tilde{E}_\theta}{B} = -\frac{imc}{rB}\tilde{\phi}_p \tag{38}$$

Here we have $\tilde{E}_\theta$ as fluctuations of the electric field and B is the axial magnetic field, the factor of c only comes from a CGS unit system and it is worth noting that this stems directly from a traditional $v_e = \frac{\boldsymbol{E}\times\boldsymbol{B}}{|B|^2}$. Substituting in our new expression for the velocity we have

$$\Gamma = \frac{3mc}{2rB} Re\{i\langle \tilde{T}\tilde{\phi}_p \rangle\} = \frac{3mc}{2rB}\int \left|P_{\phi_p T}\right| \sin\left(\Theta_{\phi_p T}\right) df \tag{39}$$

Where $P_{\phi T}$ is the amplitude of the cross-power spectrum of ϕ_p and T_e, and $\Theta_{\phi_p T}$ is the phase of the cross-power spectrum of ϕ_p and T_e, and the integral is taken over the frequency range of interest, typically between $2-3Mhz$ for ETG modes in CLM, wherever the dominant mode peak is located. By integrating only over the dominant mode peak in the fluctuation power spectrum, it is possible to isolate the transport due to the dominant ETG mode rather than simply total radial transport.

Once radial thermal conduction flux is obtained we can easily compute the radial thermal conductivity from

$$X_{e\perp} = -\frac{\Gamma}{\frac{\partial T_e}{\partial r}} \tag{40}$$

Which is the radial thermal conduction flux normalized by the gradient of temperature. To determine the gradient of temperature we can use our previous measurements of the electron temperature profile.

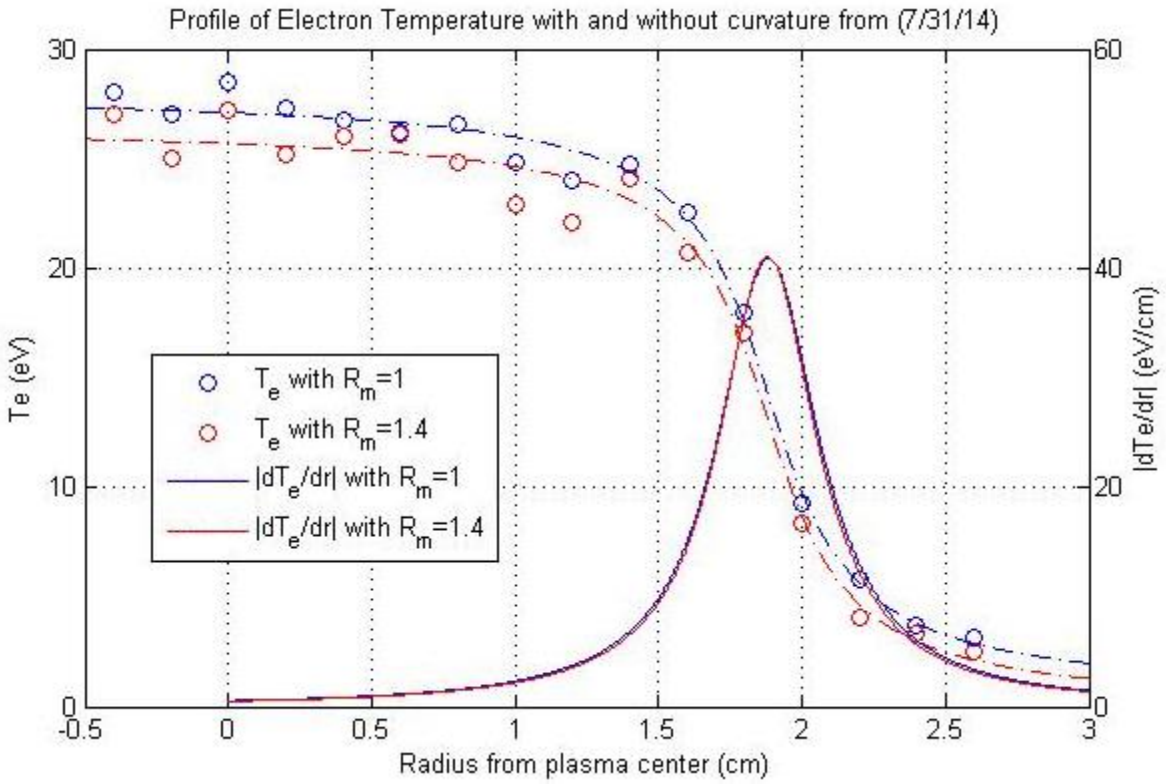

Figure 4.1: Electron Temperature T_e and $\left|\frac{\partial T_e}{\partial r}\right| = -\frac{\partial T_e}{\partial r}$ with and without curvature

Figure 4.1 shows the experimentally measured values of $-\frac{\partial T_e}{\partial r}$. We use the same fitting for temperature $T_e \cong f(x) = a * \tan^{-1}(bx + c) + d$ used in figure 3.1 to determine the value of L_{T_e}. It can be seen that despite the slight decrease in overall temperature the gradient of temperature is nearly identical with and without curvature, peaking at about $-\frac{\partial T_e}{\partial r} \sim 40 \frac{eV}{cm}$ for $r \approx 1.8\ cm$, and with a value of $-\frac{\partial T_e}{\partial r} \sim 30 \frac{eV}{cm}$ at the peak mode location of $r \approx 2.0\ cm$.

4.2 Experimental Diagnostics and Setup for Radial Transport Measurements

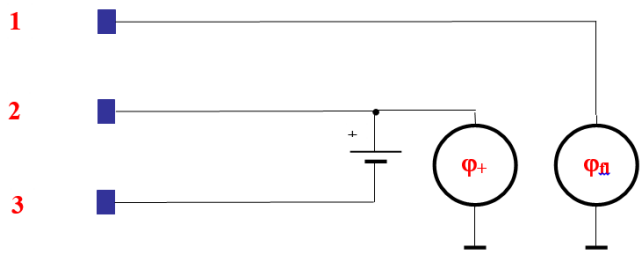

Figure 4.2: Basic Triple Probe

A standard triple probe operates as combination double probe and floating probe [52,53]. If the potential difference between the double probe tips is at least a few T_e the negative electron will draw the ion saturation current and the positive one will draw and equal and opposite current slightly above the floating potential. The third probe simply measures the floating potential. This gives 3 points on the I-V characteristic and is enough to obtain the electron temperature T_e using the approximate formula

$$T_e(eV) \approx \frac{\left(\phi^+(V) - \phi_{fl}(V)\right)}{\ln(2)} \tag{41}$$

Triple probes can measure fluctuations in temperature and potential simultaneously, and are effective for measuring radial transport. Although basic designs are suitable only for low frequency and DC measurements, modifications can be made to design probes capable of measuring high frequency and small spatial scale ETG Fluctuations [51].

In CLM we use a specially designed miniature triple probe with tungsten tips having a diameter ~ 0.2 mm, and length ~2.5 mm. For measurement of the floating potential fluctuations $\tilde{\phi}_f$ we used a blocking capacitor 0.1pF and preamplifier; therefore we have $Z_{load} > 10^6\Omega$ and bandwidth >5 *MHz*. The same circuit is used for measurement of the floating potential fluctuations

of the positive probe of a double probe $\tilde{\phi}^{+}$. To minimize noise we use miniature SMD's (surface mounted devices) for resistors and capacitors both in probes and OPAMPs.

With our probe arrangement, the temperature fluctuation of $\tilde{T}_e$ is given by [54]: $\tilde{T}_e(eV) \approx \left(\tilde{\phi}^{+}(V) - \tilde{\phi}_{fl}(V)\right) / \ln(2)$, where $\tilde{\phi}_{fl}(V)$ is the floating potential fluctuations of the single floating probe and $\tilde{\phi}^{+}(V)$ is the floating potential fluctuations of the positive side of the double probe.

This calculation can be done in near-real time and it is possible to calculate fast fluctuations in electron temperature using this method provided that the circuit has a high enough response time. In order to operate at ETG frequency and spatial scales the design has been further modified. The choice of SMD resistors and capacitors as well as the OP 2356 op-amp were made to maximize the signal-to-noise ratio while still measuring a robust signal in the ETG frequency range, nominally 2.5 MHz.

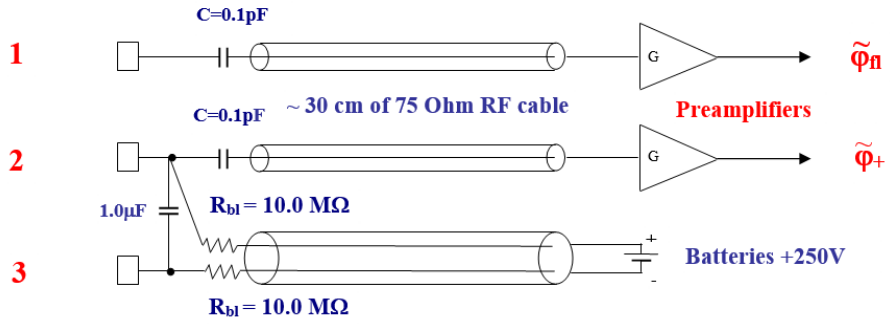

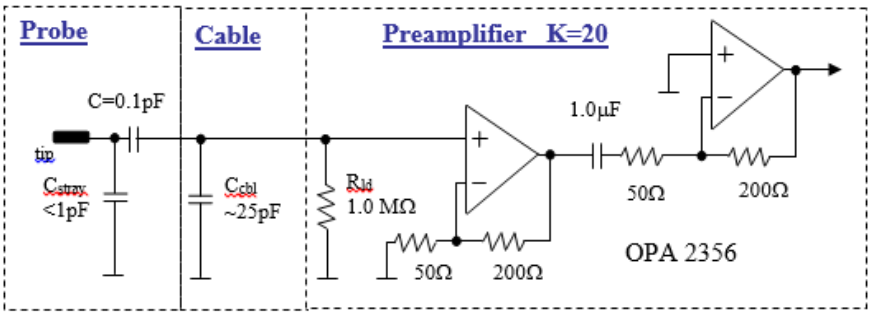

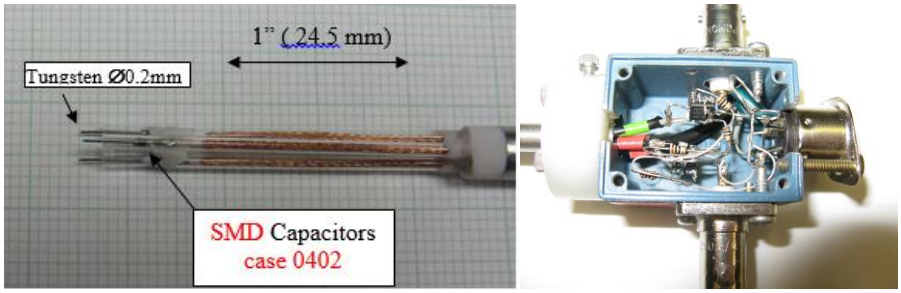

Figure 4.3: Modified High Frequency Triple Probe Design for CLM

We use same miniature preamplifiers as described in Ref [55]. The 200 MHz,CMOS operational amplifier OPA 2356 and SMD (case 0402 and 0603) components are used to create a miniature preamplifier with gain 20 and output voltage up to ± 2.5 V. This preamplifier circuit restores the amplitude of the plasma potential fluctuation signal after a capacitive divider, which is then used as a compensation signal for the energy selector grid as described above (see Fig. 4.3).

The circuit has been designed to maximize the signal to noise ratio through careful choice of capacitance values. For ETG modes in the range of $\omega \sim 2\pi * 2.5MHz$ the effective impedance of the capacitors is $R_{c=0.1pF} \sim 10^6\Omega$, $R_{c=1pF} \sim 10^5\Omega$, $R_{c=25pF} \sim 4 \cdot 10^3\Omega$. We note that for ETG frequencies the effective impedance of the cable is much smaller than the $1M\Omega$ load resistor that it is in parallel with, and the load resistor can largely be ignored.

For ETG fluctuations with $U \sim 0.3V$, the division between the $\sim .1pF$ SMD capacitors in the probe tip and the $\sim 25pF$ capacitance divided the signal seen by the first amplifier stage to $U/250 \sim 1mV$.

If we consider the noise level that will be seen by the first stage of the amplifier, we have

$$U_{noise}^2 = e_n^2 + (i_n r_{load})^2 + n_{r_{load}}^2$$

Here $e_n = 5.8\frac{nV}{\sqrt{Hz}} \sim 9\mu V$ is voltage noise from the OPA 2356 amplifier as taken from the data sheet, $i_n = \frac{50fA}{\sqrt{Hz}}$ is shot noise from the current draw of the amplifier which gets multiplied by the effective $r_{load} \sim \frac{R_{ld}R_{C_{cable}}}{\mathrm{R}_{ld}+\mathrm{R}_{\mathrm{C}_{\mathrm{cable}}}} \sim R_{C_{cable}} \sim 10^4\Omega$ resistance of the system giving $i_n r_{load} \sim .5\mu V$. In practice both of these are dominated by the Johnson-Nyquist thermal noise of the resistor $n_{r_{load}}$ which can be approximated as $n_{r_{load}} = (4k_B T\Delta f r_{load})^{1/2} \sim 13\mu V$ for a full bandwidth of $\Delta f \sim 2.5MHz$. This gives an estimate of $U_{noise} \sim 15\mu V$. A few other configurations were simulated in SPICE before settling on the current one, but we found it had the appropriate balance of minimal noise and strong signal levels. To accommodate the high frequencies involved we used our standard high speed digitizer. NI 5122, 100MS/sec, 14bits, and the probe along with the circuitry was calibrated and tested using lab-bench techniques prior to being used in the plasma.

Using this specially designed triple probe we are able to easily measure the fluctuation in electron temperature, written explicitly as:

$$Triple\ Probe\ Temperature\ Measurements: \tilde{T}_e \approx \left(\frac{e}{k}\right)\frac{\left(\tilde{\phi}_+(V) - \tilde{\phi}_{fl}(V)\right)}{\ln(2)}$$

Further details of the design can be found in All other details you can find in [56].

This specially designed high-frequency triple probe is modified to be operated on the scale of MHz, and is capable of being used for our current ETG studies in CLM.

4.2 Experimental Scaling Radial Transport Measurements

Using our triple probe diagnostics we were able to obtain levels for $\tilde{\phi}_p$, $\tilde{T}_e$ and calculate Γ for different curvature levels and initial conditions across several run days. We took $\frac{\partial T_e}{\partial r}$ to be the value at the peak of the mode $\left|\frac{\partial T_e}{\partial r}\right| \sim 3eV/cm$ for the purposes of our calculations.

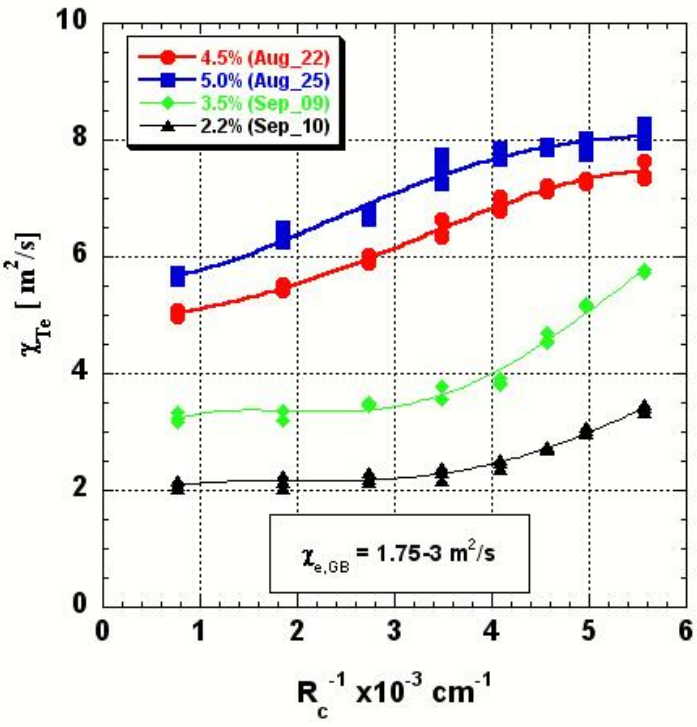

Figure 4.4: Thermal Conductivity Scaling with Curvature for different initial conditions

Figure 4.4 shows a preliminary scaling of electron thermal conductivity with curvature. For sufficiently small levels of fluctuation, the electron thermal conductivity increases roughly exponentially with curvature, similar to scaling seen by potential fluctuations. For higher fluctuation levels the electron thermal conductivity saturates around $\chi_{T_e} \sim 8.0\, m^2/s$, despite the increased potential fluctuations. Based on the potential fluctuation levels we can calculate the Gyro-Bohm diffusion coefficient for each of the curves in the slab limit [51], which vary between $\chi_{e,GB} = 1.75\, m^2/s$ for $\tilde{\phi}_p \sim .022\, T_e$ for the lowest black curve and $\chi_{e,GB} = 3\, m^2/s$ for

$\tilde{\phi}_p \sim .05\ T_e$ the largest blue curve. $\chi_{e,GB}$ scales with temperature and magnetic field, both of which are relatively stable for different curvature levels.

This is one of the first experimental results of radial thermal transport scaling as a function of curvature, resulting from a unique diagnostic and the capabilities of CLM. It shows that χ_{T_e} varies between $2 - 8\ m^2/s$ for different plasma conditions and a curvature range of $R_c^{-1} \sim .08 - .56\ m^{-1}$ in CLM, increasing up to a factor of ~2 over this range. It also indicates that the level of electron thermal conductivity χ_{T_e} can scale linearly with smaller values of potential fluctuation, but it reaches a saturated level as a function of curvature, despite the exponentially increasing potential fluctuations.

Chapter 5: Discussion and Conclusions

In this thesis we presented an overview of recent experiments of mixed slab-toroidal modes performed in CLM, and studied changes in the mode behavior and structure with increases in magnetic curvature. Summarizing our results, we found evidence of the following:

- Increases in curvature led to higher levels of saturated mode amplitude. Integrating along the full spectrum of ETG modes we found the increase in potential fluctuations to be a (~1.5x)
- We found that curvature led to a single dominant "peak" in the ETG spectrum, and the dominant peak along could increase by a factor of ~4-6 in power density (~2-2.5x in amplitude).
- We found evidence for a small increase in azimuthal wave structure on the order of $\Delta m \sim 1$ as a function of increased curvature. And although there is no theory to compare to directly, the fact that *m* is changing and the direction of the change agrees with prior simulations of ETG in CLM [20,21]
- We find evidence for small increases in real ETG frequency $\Delta\omega/\omega \sim 20\%$, which would agree with the resonance condition $\omega \sim k_{\parallel} v_{T_e}$ and the prediction from kinetic and fluid theory that $(k_{\parallel,curvature} < k_{\parallel,slab})$ [33]
- We measure higher levels of radial transport and electron thermal conductivity with increases in magnetic curvature $\frac{\chi_{T_e,curvature}}{\chi_{T_{e,slab}}} \sim 1.5 - 2.0$ which is on the order of ~2-3D_{GB}.

Overall, we have produced one of the first experimental observations of the transition between slab and mixed slab-toroidal ETG modes, characterized by increased curvature of the magnetic field lines. Although it is hard to make direct comparisons between a basic physics device like CLM and large scale advanced tokamaks, broadly speaking the changes in frequency and mode structure behave as expected from theory and simulation [21,33], and although we observe higher saturated mode amplitude, the existing theory and simulations aren't quite able to capture the behavior full behavior of CLM as a function of curvature

Speculating further, our bicoherence analysis would suggest a possible change in the mode coupling and damping, and this would be one possible cause of the changing saturated mode amplitude, but significant work would need to be done experimentally, theoretically, and numerically to understand the underlying physics and if this is actually the case. We note that the validation work for slab-ETG modes in CLM done by Fu using the GTC found almost no increase in mode amplitude when the curvature of the device was increased, although it was able to capture the changing perpendicular wave-structure.

We also have provided one of the first experimental scaling of electron thermal transport as a function of curvature. We found enhanced transport with curvature, but it was still on the order of a few D_{GB}, which would be consistent with simulations of a sheared slab-geometry and low-transport tokamaks observations. However, this doesn't rule out ETG producing much larger transport under different circumstances, and further investigations of the interplay between ETG driven transport and curvature may be a fruitful area of research for other basic experiments and confinement concepts.

References

[1] G. G. Howes, S. C. Cowley, W. Dorland, G. W. Hammett, E. Quataert, and A. A. Schekochihin, Astrophys. J. 651, 590 (2006).

[2] P. Fauchais, J. Phys. D 37, R86 (2004)

[3] G. R. Tynan, A Fujisawa, and G. McKee, Plasma Phys. Controlled Fusion 51, 113001 (2009)

[4] E. J. Doyle, W.A. Houlberg et. al., Nucl. Fusion 47 S18 (2007)

[5] W. Horton, B. G. Hong and W. M. Tang, Phys. Fluids 31 (10), 2971 (1988)

[6] R. E. Waltz, J. Candy and M. Fahey, Phys. Plasmas 14, 056116 (2007)

[7] W. Dorland, F. Jenko, M. Kotschenreuther and B. N. Rogers, Phys. Rev. Lett. 85, 5579 (2000)

[8] Z. Lin, L. Chen and F. Zonca, Phys. Plasmas 12, 056125 (2005)

[9] W. M. Nevins et al., Phys. Plasmas 13, 122306 (2006)

[10] F. Jenko, W. Dorland et al., Phys. of Plasmas 7, 1904 (2000)

[11] W. M. Nevins et al., Phys. Plasmas 13, 122306 (2006)

[12] E. Mazzucato et al., Phys. Rev. Lett. 101, 075001 (2008)

[13] C. Holland and P. H. Diamond, Phys. of Plasmas, **11** (2004)

[14] Z. Lin, L. Chen and F. Zonca, Phys. Plasmas 12, 056125 (2005

[15] E. Z. Gusakov et al., Plasma Phys. Controlled Fusion 48, A371 (2006)

[16] L. Schmitz et al., Phys. Rev. Lett. 100, 035002 (2008)

[17] E. Mazzucato et al., Phys. Rev. Lett. 101, 075001 (2008)

[18] T. Gorler and F. Jenko, Phys. Rev. Lett. **100** 185002 (2008)

[19] L. Schmitz, C. Holland et. al., Nucl. Fusion **52** (2012)

[20] X. Wei, V. Sokolov, A.K. Sen, Phys. of Plasmas 17 042108 (2010)

[21] X. R. Fu, W. Horton, Y. Xiao et al., Phys. of Plasmas **19**, 032303 (2012)

[22] I. Holod, W. L. Zhang, Y. Xiao, and Z. Lin, Phys. Plasmas **16**(12), 122307 (2009)

[23] S. K. Mattoo, S. K. Singh, L. M. Awasthi, R. Singh, and P. K. Kaw, Phys. Rev. Lett. 108, 255007 (2012)

[24] S. K. Singh, L. M. Awasthi, S. K. Mattoo, R. Singh, and P. K. Kaw, Plasma Phys. Control. Fusion **54** 124015 (2012)

[25] Chanho Moon, Toshiro Kaneko and Rikizo Hatekeyama, Phys. Rev. Lett. **111**, 115001 (2013)

[26] J.C. Hillesheim, J. C. DeBoo, W. A. Peebles et. al., Phys. Rev. Lett **110**, 045003 (2013)

[27] J. C. Hillesheim, J. C. DeBoo, W. A. Peebles et. al. Phys. Plasmas **20**, 056115, (2013)

[28] C. Holland, J. E. Kinsey, et. al. Nucl. Fusion, **53** 083027

[29] W. Horton, Rev. of Modern Physics **71**, 735-778 (1999)

[30] G. R. Tynan, A. Fujisawa, G. McKee, Plasma Phys. Control. Fusion **51**, 113001, (2009)

[31] T. H. Stix, *Waves in Plasmas*, (American Institute of Physics, New York NY, 1992)

[32] R. J. Goldston and P. H. Rutherford *Introduction to Plasma Physics,* (Taylor and Francis Group, New York NY, 1995)

[33] J. Kim and W. Horton, Phys. Fluids B **3**, 1167 (1991)

[34] Y. C. Lee, J. Q. Dong et al., Phys. Fluids **30**, 1331, (1987)

[35] W. Horton, B. G. Hong and W. M. Tang, Phys. Fluids **31**, 2971 (1988)

[36] F. Jenko, W. Dorland and G. W. Hammett, Phys. of Plasmas 8, 4096 (2001)

[37] V. Sokolov and A.K. Sen, Phys. Rev. Lett. **107**, 155001 (2011)

[38] E. K. Tokluoglu, V. Sokolov and A. K. Sen, Phys. Plasmas **19** 102306 (2012)

[39] E Z Gusakov, A D Gurchenko et. al. Plasma Phys. Control. Fusion **48** A371 (2006)

[40] E. Mazzucato, R. E. Bell, S. Ethier et. al., Nuclear Fusion **49** 055001 (2009)

[41] J. Chen, A. K. Sen, Phys. Rev. Lett. **72**, 3997 (1994)

[42] J. Chen, A. K. Sen, M. Mauel, Phys. Rev. Lett. **66** 429 (1991)

[43] S. C. Prager, T. C. Marshal and A. K. Sen Plasma Physics **17** 785 (1975)

[44] R. Scarmozzino, A. K. Sen, and G. A. Navratil, *Phys. Fluids* **31** (6), 1773 (1988)

[45] I. H. Hutchinson, *Principles of Plasma Diagnostics, (*Cambridge University Press, New York NY, 2002)

[46] N. Hershkowitz, *Plasma Diagnostics*, (Academic Press, San Diego CA, 1989)

[47] Y. Nagashima, S. –I. Itoh, et. al, Rev. Sci. Instrum. **77** 045110 (2006)

[48] V. Sokolov and A. K. Sen, Phys. Rev. Lett. 113, 095001 (2014)

[49] J. Chen and A. K. Sen, Physics of Plasmas **2**, 3063-3070 (1995)

[50] J. S. D.W.Ross, *Plasma Phys. and Control.Fusion* **34**, 137 (1992)

[51] V.Sokolov, and A.K.Sen, *Phys. Rev. Lett.* **107**, 155001 (2011)

[52] S. Chen, and T. Sekiguchi, *J. Appl. Phys.* **36**, 2363 (1965);

[53] H. Y. W. Tsui, R. D. Bengston, G. X. Li, et al, Rev. Sci. Instrum. **63**, 4608 (1992)

[54] H. Y. W. Tsui, R. D. Bengston, G. X. Li, et al, Rev. Sci. Instrum. **63**, 4608 (1992).

[55] V.Sokolov, and A.K.Sen, *Rev. Sci. Instrum.* **83,** 103503 (2012)

[56] V,Sokolov *Rev. Sci. Instrum.* submitted on December 2014